RESEARCH ARTICLE | NOVEMBER 03 2023

Numerical study of inflow turbulence distortion and noise for airfoils

André F. P. Ribeiro ; Fernanda L. dos Santos ; Kees Venner ; Leandro D. de Santana

Physics of Fluids 35, 115112 (2023)
https://doi.org/10.1063/5.0169000

Physics of Fluids ARTICLE pubs.aip.org/aip/pof

Numerical study of inflow turbulence distortion and noise for airfoils

Cite as: Phys. Fluids **35**, 115112 (2023); doi: 10.1063/5.0169000
Submitted: 22 July 2023 · Accepted: 13 October 2023 ·
Published Online: 3 November 2023

André F. P. Ribeiro,[1] Fernanda L. dos Santos,[2,a)] Kees Venner,[2] and Leandro D. de Santana[2]

AFFILIATIONS

[1]SIMULIA, Dassault Systemes GmbH, Meitnerstrasse 8, Stuttgart, Germany
[2]Department of Thermal Fluid Engineering, University of Twente, Drienerlolaan 5, Enschede, The Netherlands

[a)]Author to whom correspondence should be addressed: f.l.dossantos@utwente.nl

ABSTRACT

In this work, the interaction of grid-generated turbulence with airfoils of different thicknesses, namely, a National Advisory Committee for Aeronautics (NACA) 0008 and a NACA 0018, is investigated, leading to a deeper understanding of the influence of the airfoil geometry on the near-field flow and on the far-field pressure fluctuations. Experimentally validated lattice-Boltzmann simulations are used to analyze the flow properties in the leading-edge (LE) vicinity. The analysis of the velocity fluctuations near the LE shows that momentum is transferred from the streamwise to the transverse velocity for the NACA 0008 airfoil interacting with a large turbulence length scale. This mechanism changes with the increase in the airfoil thickness because the inflow turbulence length scale becomes comparable to the airfoil thickness in the LE region, resulting in a higher concentration of vortices near the LE oriented in the transverse direction, creating high-velocity fluctuations in the spanwise direction. The near- and far-field pressure fluctuations are analyzed to understand the impact of the inflow turbulence distortion on these parameters and the limitations of analytical methods for real airfoils. Results show that the wall-pressure fluctuations are affected by the turbulence distortion in the LE region. Thick airfoils have noise directivity patterns significantly different compared to the Amiet predictions for higher frequencies, radiating higher noise levels upstream of the LE than the thin airfoil. This is likely associated with a drastic change in the pressure fluctuation distribution near the airfoil LE region, attributed to the change in the distortion of the vortical structures in the LE area.

NOMENCLATURE

CAA	computational aeroacoustics
CFD	computational fluid dynamics
Cp	pressure coefficient
c	airfoil chord
c_∞	speed of sound
$\vec{c}$	particle velocity vector
DNS	direct numerical simulation
D_H	wind tunnel hydraulic diameter
d	airfoil span
FW–H	Ffowcs Williams–Hawkings
f	frequency
G_{pp}	one-sided pressure power spectrum density at an observer position
G_{qq}	one-sided pressure power spectrum at airfoil surface
g	airfoil response function
g^*	complex conjugate of airfoil response function
ILES	implicit large eddy simulation
K_x	specific streamwise wavenumber
K_y	specific spanwise wavenumber
k_e	wavenumber scale of largest eddies
k_x	streamwise wavenumber
k_y	spanwise wavenumber
$\mathscr{L}$	aeroacoustic transfer function
L	loading source term
LBM	lattice-Boltzmann method
LE	leading edge
LES	large eddy simulation
M	Mach number
N8	NACA 0008 airfoil
N18	NACA 0018 airfoil
NS	Navier–Stokes
PSD	power spectral density

p	pressure
q	dynamic pressure
RDT	rapid distortion theory
RMS	root mean square
r	radius
$_{\text{ref}}$	reference value taken at an arbitrary location
$_{\text{rms}}$	root mean square quantity
t	time
$t_{\max}$	maximum airfoil thickness
u	streamwise flow velocity
$\bar{u}$	mean streamwise flow velocity
VLES	very large eddy simulation
v	spanwise flow velocity
vK	von Kármán
WPF	wall pressure fluctuations
w	transverse flow velocity
x	streamwise position
$\vec{x}$	position vector
y	spanwise position
z	transverse position
Λ_f	streamwise turbulence integral length scale
Δt	time step duration
$\Delta\bar{u}$	difference between the streamwise mean velocity of a case with and without an airfoil
$\Delta\Lambda_f$	difference between streamwise turbulence integral length scale of a case with and without an airfoil
$\Lambda_{f,0}$	streamwise turbulence integral length scale at the position of the airfoil leading edge, but in the empty wind tunnel
Λ_g	transverse turbulence integral length scale
ρ	fluid density
σ^2	$x_o^2 + (1 - M^2)(y_o^2 + z_o^2)$
Φ_{uu}	streamwise turbulence spectrum
Φ_{ww}	transverse turbulence spectrum
φ	particle distribution function
$_o$	observer position
$_\infty$	freestream quantity

I. INTRODUCTION

Flow-induced noise negatively impacts people and wildlife,[1–4] being a relevant problem to the sustainable development of ships, aircraft engines, and wind turbines. Leading-edge (LE) noise is an important low-frequency sound production mechanism,[5] occurring in situations such as blade interaction with the wake generated by a ship hull, a stator crossing the wake generated by a rotor, or the atmospheric boundary layer impinging on a wind turbine blade. The phenomenon is caused by fluctuations in the incoming flow impinging on the LE of the blades, leading to wall-pressure fluctuations (WPF) and hence noise radiation to the far field. LE noise is relevant for noncavitating marine applications since low-frequency sound waves can propagate over large distances due to higher sound speed in water compared to air and low sound absorption,[6,7] harming marine animals that depend on sound for communication, mating, searching for prey, and avoiding predators.[3,4] Therefore, understanding the LE noise mechanism is crucial to developing accurate noise prediction methods and technologies to mitigate LE noise production. The typical nomenclature used for LE noise, which we use throughout this work, is shown in Fig. 1, where the origin of the coordinate system is considered at the airfoil LE at mid-span.

The blade geometry is a critical parameter for the LE noise generation.[8–13] Among the airfoil geometrical parameters, the airfoil LE region has the most significant influence on this noise source.[12,14,15] The airfoil camber is reported to have a small effect on the radiated LE noise.[8,9,16] The angle of attack also has negligible influence in the LE noise generation.[8,9,16,17] Moreau *et al.*[9] found that LE noise is insensitive to changes in the angle of attack from zero to 15°. Gill *et al.*[12] and Hainaut *et al.*[14] used computational aeroacoustics (CAA) to study the main airfoil geometrical parameters influencing LE radiated noise. Gill *et al.*[12] considered single-frequency harmonic gusts interacting with the LE of symmetric airfoils of different thicknesses and LE nose diameters. Hainaut *et al.*[14] considered two-component synthetic turbulence and investigated the inflow turbulence interaction with the LE of symmetric airfoils of several LE nose diameters, chord lengths, thicknesses, and maximum thickness locations. Gill *et al.*[12] showed that the airfoil maximum thickness and LE nose diameter affect the radiated noise, resulting in lower sound power levels as these parameters increase, mainly for high frequencies. Paruchuri[16] came to the same conclusion in an experimental study. Hainaut *et al.*[14] observed the same trend for an observer position normal to the airfoil. Hainaut *et al.*[14] showed that the location of maximum thickness also influences the LE noise, resulting in higher noise levels for high frequencies as the location of maximum thickness shifts downstream. They investigated the effect of the chord length on LE noise by keeping the geometry upstream of the maximum thickness the same and changing the geometry downstream of this location. They reported that the chord length did not affect the LE noise and concluded that the LE noise is only influenced by the geometry forward of the position of the maximum thickness.

According to Gill *et al.*[12] and Hainaut *et al.*,[14] the mechanism responsible for the effect of the airfoil geometry on the LE noise is the distortion of the inflow turbulence as it approaches the LE. Gill *et al.*[12] attributed this turbulence distortion to the velocity gradients in the LE stagnation region, which resulted in a larger stagnation region for airfoils with a larger thickness. However, the specific mechanism responsible for the turbulence distortion near an airfoil LE has not been extensively investigated yet.[18,19] According to the rapid distortion theory (RDT) developed by Hunt,[20] the mechanism responsible for the turbulence distortion in the stagnation region of a cylinder depends on the ratio of the cylinder radius r to the turbulence integral length scale Λ_f.[21] This dependence is assumed to also occur in the case of turbulence–airfoil interaction because, according to Mish and Devenport,[22] the inflow distortion produced by an airfoil in the region sufficiently close to the stagnation point is similar to that produced by a cylinder with a radius equal to the airfoil LE radius. According to the RDT, for $\Lambda_f \gg r$, the governing physical mechanism of the turbulence

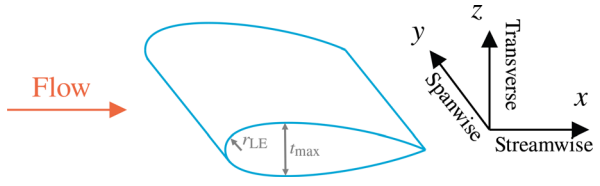

FIG. 1. Nomenclature used throughout the paper, where r_{LE} is the leading-edge radius and t_{max} is the airfoil maximum thickness.

distortion is the flow blockage imposed by the cylinder.[20,21] This yields a momentum transfer between the streamwise and the upwash velocity (z direction) as the flow approaches the cylinder LE along the stagnation streamline. As a result, the root mean square (RMS) of the streamwise velocity fluctuations u_{rms} decreases, and the RMS of the transverse velocity fluctuations w_{rms} increases close to the body LE, whereas the RMS of the spanwise velocity fluctuations v_{rms} remains constant. For $\Lambda_f \ll r$, the turbulence distortion is caused by the mean velocity field, which stretches and rotates vortex lines, resulting in the distortion of the vorticity field and consequent change of the turbulent velocities.[20,21] In that case, the opposite behavior is observed: the u_{rms} and the w_{rms} values increase and decrease, respectively, close to the body LE.

Recent experimental studies[23–26] have focused on LE noise and turbulence distortion for airfoils. However, in experiments, measuring the noise of an airfoil under homogeneous grid-generated turbulence is challenging because the noise created by the grid is often comparable to the LE noise. Also, measuring and analyzing the turbulence distortion very close to the LE are difficult because not all flow properties can be measured simultaneously at several locations. Furthermore, the measurement itself may be intrusive and can modify the flow it aims to measure. In this context, numerical studies can complement experimental investigations because they result in the complete and simultaneous flow field, allowing a more in-depth analysis of the turbulence distortion phenomenon.

Numerical simulations of freestream turbulence impinging on an airfoil LE have historically been carried out assuming inviscid flow, using vortex methods[27,28] or Euler-based methods.[29–31] Although LE noise caused by interaction with blade wakes, e.g., a rotor–stator configuration, has been studied in depth with high-fidelity computational fluid dynamics (CFD),[32] LE noise due to interaction with a wind/water-like turbulence spectrum, as experienced by wind turbines and ship propellers, has rarely been directly simulated with such methods.[33,34] These high-fidelity simulations allow the inclusion of potential boundary layer effects on LE noise and any interaction with flow separations and trailing-edge noise. For the specific case of the turbulence distortion mechanism, this phenomenon has been investigated numerically by Gill *et al.*[12] and Hainaut *et al.*,[14] where they investigated one- and two-dimensional disturbances, respectively, interacting with airfoil geometries. However, according to Gill *et al.*,[12] studying the turbulence distortion for a realistic turbulent inflow containing three-dimensional disturbances is paramount because the turbulence may be deformed differently than one-dimensional or two-dimensional disturbances. Thus, high-fidelity simulations of realistic inflow turbulence interacting with airfoils can yield valuable results to investigate the turbulence distortion phenomenon, complementing the experimental investigations.

The current study investigates the turbulence distortion for different airfoil geometries numerically. The main objective is to deepen our understanding of the inflow turbulence distortion mechanism near the LE of airfoils. A secondary objective is to understand the effects of airfoil thickness on the turbulence distortion phenomenon, including the pressure fluctuations on the airfoil surface and in the far field. Both objectives are achieved using a realistic turbulent inflow containing three-dimensional, broadband disturbances. In this work, the lattice-Boltzmann method (LBM) is used. The numerical methodology is first validated by comparing the numerical results of grid-generated turbulence with experimental data available in the literature. Throughout this work, we use the word "grid" to refer to the turbulence generation device in the wind tunnel and "mesh" as the set of elements that discretize the fluid domain in the simulation. We perform simulations of the grid-generated turbulence interacting with a National Advisory Committee for Aeronautics (NACA) 0008 airfoil to validate the flow properties near the LE with experimental data. After validating the simulation method, we investigate the turbulence distortion mechanism for two airfoils, a NACA 0008 and a NACA 0018, based on the flow field near the LE region. Subsequently, we analyze the simulated spectrum of the WPF and far-field noise of the airfoils, comparing these results with the predictions of semi-analytical models and experimental data when available. Finally, we investigate the thickness effects on the far-field noise directivity pattern for different frequencies.

II. NUMERICAL METHODS

A brief summary of the numerical methods used in this work is given in this section. Detailed information on the flow solver and noise propagation approach is given in the references.

A. Fluid solver

In the last two decades, the LBM[35] has become a viable alternative to perform high-fidelity simulations. Unlike the classic simulations based on Navier–Stokes (NS) equations, instead of using continuum mechanics as the foundation to describe fluid flow, the LBM uses statistical mechanics, considering the fluid as particles that interact with each other and the boundary conditions.

The method uses the particle distribution function $\varphi(\vec{x}, \vec{c}, t)$, which represents the probability that particles at position $\vec{x}$ and time t have velocity $\vec{c}$. Discretizing space into a numerical mesh, time into a finite time step Δt, and the velocity space into a finite number of possible velocities (i.e., using a discrete velocity method[36]), the discrete Boltzmann equation can be numerically solved,[37] leading to the lattice-Boltzmann equation. Eddy viscosity can be added to the fluid viscosity in the particle collision model if turbulence modeling is used. With φ computed, fluid properties can be extracted from its moments, and pressure is calculated based on the ideal gas law.

A key feature of the LBM is that fluid advection is achieved by directly moving particle density functions from one cell to another without using costly and dissipative interpolation functions. The collision step accounts for the interaction between particles with different velocities in the same cell. This is usually computed with the Bhatnagar–Gross–Krook (BGK)[38] approximation, which only depends on simple mathematics based on local quantities, making it computationally inexpensive and well-suited for parallelization, unlike the derivatives in the NS equations.

The LBM computations are conducted with PowerFLOW®, a commercial CFD code, which is able to handle very complex geometries[39] by using a Cartesian mesh and the concept of surface elements, or surfels.[40] Due to the Cartesian mesh, a wall model is necessary, which is done similarly to NS solvers by employing the log-law and pressure gradient corrections.[41] In addition, the solver is usually run using very large-eddy simulations (VLES), which allow for a hybrid approach of Reynolds-averaged Navier–Stokes (RANS) and large-eddy simulations (LES).[42] Here, we are interested in resolved turbulence, mainly the free-stream turbulence; therefore, we avoid turbulence modeling strategies away from the walls. Hence, the LBM simulations

are conducted as coarse direct numerical simulations (DNS) or implicit LES (ILES), meaning that the numerical dissipation of the numerical method and mesh act as a sub-grid-scale model.[43] This was achieved by multiplying the eddy viscosity by zero in the simulations included herein.

The LBM can formally reproduce the physics of the weakly compressible NS equations,[44] depending on the discretization of the velocity space,[45] equilibrium distribution function,[46] and collision model,[38] while presenting potential advantages in terms of computational performance and numerical dissipation. For aeroacoustics, in particular, LBM exhibits low-dissipation characteristics equivalent to high-order methods,[47] while the explicit and simple mathematics of the algorithm can make it substantially faster than NS methods[48] when small time steps are used. For aerodynamics, the performance advantage can be reduced,[49] especially as NS solvers can use larger time steps.[50] Some relevant applications of the LBM for this paper are simulations of the wake of a cylinder impinging on another cylinder in an open jet wind tunnel,[51] unsteady airfoil aerodynamics,[52] and applications to airfoil trailing-edge noise using DNS,[53] ILES,[54] and VLES.[55]

B. Noise propagation

Numerical approaches can successfully compute pressure fluctuations, i.e., noise, in arbitrary locations of the computational domain. However, it is prohibitively expensive to represent the propagation of the noise sources to the targets, i.e., microphones, with high resolution. Therefore, acoustic analogies are powerful tools for predicting far-field noise based on near-field pressure fluctuations. Therefore, this paper adopts the Ffowcs Williams–Hawkings (FW–H) acoustic analogy coupled to the LBM.[56]

The FW–H analogy[57] considers a surface near the acoustic sources to propagate the aeroacoustic noise to arbitrary points in space. The surfaces can coincide with solid walls or be placed arbitrary around them, yielding approaches dubbed as solid or permeable, respectively. The formulation is based on a rearrangement of the Navier–Stokes equations and is often solved by neglecting viscous terms and quadrupole sources outside the surface, using the Farassat 1A[58,59] formulation, and an advanced time approach.[60] For details on the Farassat formulation 1A, see Farassat.[61]

Recent studies have shown that the solid formulation often shows severe issues, particularly with complex flows and geometries, and hence should be adopted with caution.[62] However, the permeable formulation is deemed particularly challenging for the objectives of this study. This conclusion is based on the observation that the upstream turbulence yields hydrodynamic fluctuations on the permeable data surface that would be computed as acoustic noise in the far-field microphones. Hence, we use the solid formulation, which has been used successfully for airfoil trailing-edge noise in the past.[53–55]

III. AMIET THEORY FOR LEADING-EDGE NOISE

This section briefly describes the Amiet model for LE noise and WPF because they are used to predict the WPF and far-field noise spectra for the cases investigated in this study. The reader is referred to Amiet[63] and de Santana[64] for a detailed derivation of the following expressions.

A. Far-field noise model

Amiet[63] proposed a semi-analytical model to predict the far-field noise generated by the interaction of a turbulent uniform inflow. The approach considers a flat plate of infinitely large span and negligible thickness; therefore, neglecting important effects present in airfoils of realistic geometry. The model assumes a stationary observer and frozen turbulence and is formulated in the Fourier domain. The one-sided power spectral density (PSD) of pressure fluctuations observed in the far field at position (x_o, y_o, z_o) for a flat plate of chord c and span d as a function of frequency f is

$$G_{pp}(x_o, y_o, z_o, f) = 4\pi^2 \left(\frac{2\pi f z_o \rho (c/2)}{c_\infty \sigma^2}\right)^2 \bar{u}_\infty \frac{d}{2} \left|\mathscr{L}(x_o, K_x, K_y)\right|^2 \Phi_{ww}(K_x, K_y), \quad (1)$$

where $\sigma^2 = x_o^2 + (1 - M^2)(y_o^2 + z_o^2)$, $K_x = 2\pi f / \bar{u}_\infty$, and $K_y = (2\pi f y)/(c_\infty \sigma)$. $\mathscr{L}$ is the aeroacoustic transfer function. Its formulation and derivation are shown in pages 155, 166, and 168 of the work by de Santana.[64] The main input for the Amiet prediction model is the transverse turbulence spectrum Φ_{ww}, which is discussed in Sec. III C.

B. Wall-pressure fluctuation model

In the derivation of the far-field noise model, Amiet[63] defines the two-sided cross-PSD of the surface pressure jump. Paterson and Amiet[17] show that the cross-PSD of the WPF is derived from the surface pressure jump, i.e., Eq. (18) in Paterson and Amiet.[17] From this equation, the one-sided auto-PSD at the chordwise position x as a function of frequency f is computed as

$$G_{qq}(x, f) = 8\pi \bar{u}_\infty (\pi\rho)^2 \int_0^\infty \Phi_{ww}(K_x, k_y) g(x, K_x, k_y) g^*(x, K_x, k_y) \mathrm{d}k_y, \quad (2)$$

where k_y is the spanwise wavenumber. The airfoil response function g is determined from Mish and Devenport,[65] and g^* refers to the complex conjugate of the function g.

C. Inflow turbulence spectrum models

Different models exist to represent the inflow turbulence spectrum. Two formulations for Φ_{ww} are used in this research: the traditional von Kármán turbulence spectrum and the RDT-based turbulence spectrum. These two formulations are discussed in Secs. III C 1 and III C 2. They are determined by integrating the energy spectrum function $E(k)$. A detailed derivation of this formulation is given in Glegg and Devenport[66] for the von Kármán spectrum and in de Santana *et al.*[25] and dos Santos *et al.*[24] for the RDT-based spectrum.

1. von Kármán turbulence spectrum

The inflow turbulence spectrum of the z-direction velocity is usually assumed to be represented by the two-dimensional von Kármán turbulence spectrum

$$\Phi_{ww}^{\mathrm{vK}}(k_x, k_y) = \frac{4}{9\pi} \frac{u_{\mathrm{rms}}^2}{k_e^2} \frac{(k_x/k_e)^2 + (k_y/k_e)^2}{\left[1 + (k_x/k_e)^2 + (k_y/k_e)^2\right]^{7/3}}, \quad (3)$$

where k_x is the streamwise wavenumber and k_e is the wavenumber scale of the largest eddies[66]

$$k_e = \frac{\sqrt{\pi}\,\Gamma(5/6)}{\Lambda_f\,\Gamma(1/3)}. \tag{4}$$

The von Kármán one-dimensional inflow turbulence spectrum for the streamwise velocity $\Phi_{uu}(k_x)$ is useful as a reference to validate the experimental and numerical spectra. This turbulence spectrum is given as

$$\Phi_{uu}^{\mathrm{vK}}(k_x) = \frac{2}{\sqrt{\pi}}\frac{\Gamma(5/6)}{\Gamma(1/3)}\frac{u_{\mathrm{rms}}^2}{k_e}\left[1+\left(\frac{k_x}{k_e}\right)^2\right]^{-5/6}. \tag{5}$$

It is clear from this equation that the von Kármán spectrum follows a $-5/3$ power law in k_x at high frequencies.

2. RDT-based turbulence spectrum

To account for the turbulence distortion, de Santana *et al.*[25] proposed a modification to the turbulence energy spectrum based on the asymptotic results of the RDT developed by Hunt[20] for turbulent flow around two-dimensional bluff bodies. In the proximity of an upstream cylinder wall, the decay of the one-dimensional turbulence energy spectrum $\Phi_{ww}(k_x)$ tends asymptotically to a $-10/3$ power law at high frequencies. de Santana *et al.*[25] proposed an energy spectrum formulation that results in an expression for $\Phi_{ww}(k_x)$ that follows this $-10/3$ power law at high frequencies. The resulting turbulence spectrum is given as[25]

$$\Phi_{ww}^{\mathrm{RDT}}(k_x,k_y) = \frac{91}{36\pi}\frac{u_{\mathrm{rms}}^2}{k_e^2}\frac{(k_x/k_e)^2+(k_y/k_e)^2}{\left[1+(k_x/k_e)^2+(k_y/k_e)^2\right]^{19/6}}. \tag{6}$$

The one-dimensional inflow turbulence spectrum for the streamwise velocity is[24]

$$\Phi_{uu}^{\mathrm{RDT}}(k_x) = \frac{91}{36\sqrt{\pi}}\frac{\Gamma(5/3)}{\Gamma(19/6)}\frac{u_{\mathrm{rms}}^2}{k_e}\left[1+\left(\frac{k_x}{k_e}\right)^2\right]^{-5/3}. \tag{7}$$

It is clear that the one-dimensional wavenumber for the streamwise velocity $\Phi_{uu}(k_x)$ follows a $-10/3$ power law at high frequencies as $\Phi_{ww}(k_x)$ shown by Hunt.[20]

In this study, Eqs. (3) and (6) are used as input in the Amiet models [Eqs. (1) and (2)]. Equation (5) is compared to the velocity spectrum obtained from the simulation results and is present as a function of frequency f. Thus,

$$\Phi_{uu}(f) = (2\pi/\bar{u}_\infty)\Phi_{uu}(K_x). \tag{8}$$

IV. SETUP DESCRIPTION

A. Wind tunnel reference case

The case studied in this work corresponds to an open-jet setup of a turbulent inflow impinging on an airfoil LE. The setup corresponds to the open test section of the Aeroacoustic Wind Tunnel of the University of Twente, an open-jet, closed-circuit facility with contraction with a ratio of 10:1. After the contraction, the flow enters a closed test section and subsequently an open test section. The generated uniform flow has turbulence intensity below 0.08%.[67] An anechoic chamber of $6\times6\times4$ m^3 encloses the test region. The test section dimensions are 0.7×0.9 m^2 (height $\times$ width). The airfoil is mounted vertically on the open test section, which consists of horizontal side plates; see Fig. 2.

The turbulent inflow is generated by a mono-planar rectangular grid placed in the closed test section at 1.39 m upstream of the airfoil LE; see Fig. 2. The bar width is 32 mm, and the gaps are 109.5 mm, resulting in a porosity of 60%. The turbulent flow generated by the grid was characterized experimentally using hot-wire anemometry by dos Santos *et al.*[23] The turbulence generated by the simulation is compared with the experimental results in dos Santos *et al.*[23] to validate the simulation. To do so, a simulation with an empty test section, i.e., without the airfoil, was performed.

The grid-generated turbulent inflow at the stagnation line of a NACA 0008 airfoil was evaluated by dos Santos *et al.*[24] They measured the streamwise velocity at the stagnation streamline of the airfoil using hot-wire anemometry for streamwise positions $x/r_{\mathrm{LE}} \in [-100,-1.8]$, with $x=0$ at the LE position. They also measured the WPF along the airfoil chord, with the first measurement at $x/c = 0.0007$. These experimental data sets are compared with the simulation results for a Reynolds number based on the airfoil chord of 500 000.

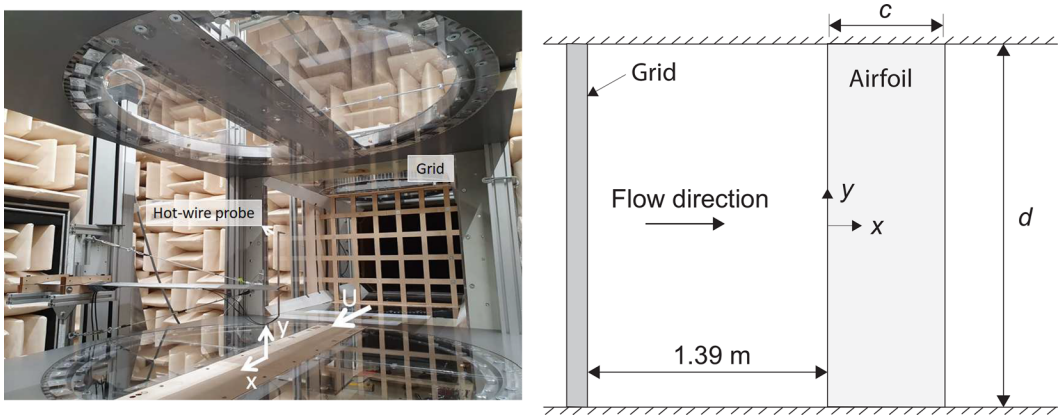

FIG. 2. Wind tunnel setup with the grid installed in the closed test section and the hot-wire probe used to characterize the turbulent flow generated by the grid.

TABLE I. Geometric parameters of the airfoils used in this research.

Airfoil	c (mm)	r_{LE}/c (-)	t_{max}/c (-)	x_{tmax}/c (-)	d/c (mm)
NACA 0008	300	0.007	0.08	0.3	2.3
NACA 0018	300	0.036	0.18	0.3	2.3

B. Numerical case setup

The airfoils NACA 0008 and NACA 0018 are used in this study to investigate the influence of the airfoil geometry on the turbulence distortion mechanism and radiated LE noise. Experimental data for the NACA 0008 airfoil are available in the literature[24] for validation. Table I shows the airfoil main geometrical parameters, namely, chord c, LE radius r_{LE}, airfoil maximum thickness t_{max}, chordwise position of the maximum thickness x_{tmax}, and span d. As the thickness in the LE region is the most critical parameter for the LE noise, two airfoils from the same family but with relatively different thicknesses were chosen.

The open jet wind tunnel was reproduced in the simulations for better comparisons with experimental data. The experimental anechoic chamber was replaced with a large cubic domain of side $200c$ with sponge zones, which are regions of high viscosity, to avoid reflections. An inlet of uniform constant velocity of about 25 m/s was placed $1.6D_H$ upstream of the turbulence grid, where D_H is the wind tunnel hydraulic diameter. In the far field, atmospheric pressure is defined as the boundary condition. Figure 3 shows the spanwise vorticity and the open jet setup. Note that the computational mesh was coarsened outside the jet shear layer and downstream of the airfoil trailing-edge. This can be noticed by the nonphysical turbulence dissipation downstream of the airfoil. The coordinate system is shown in Fig. 3, with the streamwise component of the flow being parallel to the x-axis direction, the spanwise direction parallel to the y axis, and the transverse component parallel to z axis. The origin of the coordinate system is considered at the airfoil LE position at mid-span. Figure 3 also displays the turbulence decay from the start of the open test section to the airfoil LE.

The computational mesh was kept at a constant resolution, with a cell size of $0.0373\,\Lambda_{f,LE}$, in most of the test section, from the near wake of the turbulence grid to the airfoil. This was shown to preserve the turbulence spectrum up to frequencies above 1 kHz, which is adequate for the scales of interest in this study. The local time step in this region was equivalent to 276 kHz, far exceeding time resolution requirements for the turbulence structures around 1 kHz. The mesh was further refined near the grid to capture the relevant geometrical features, with about 22 cells over the edge of the grid, transitioning to about 60 cells over the grid bar width, doubling that cell size in the near wake of the grid, and doubling the cell size again in the bulk of the flow, between the grid and airfoil. The mesh and the instantaneous spanwise vorticity field near the grid are shown in Fig. 4.

Near the airfoil LE, two levels of mesh refinement were added so that the gradients in flow quantities, such as velocity and velocity fluctuations, could be properly measured near the stagnation point. The average y^+ value on the surface of the airfoil was about 40, which is compatible with the wall model used. The airfoil trailing-edge is refined by three levels relative to the freestream mesh to resolve the trailing-edge thickness with two elements. This is sufficient, based on previous experience, due to the use of the wall model. The airfoil boundary layer was refined by one level to capture the airfoil geometry adequately. However, the boundary layer was not fully resolved in the simulations. This decision is supported by the fact that the boundary layer mainly affects trailing-edge noise, having a minor influence on LE noise. The mesh and the instantaneous spanwise vorticity field near the airfoil are shown in Fig. 5. On the right side of the image, coarsening of the mesh can be observed past the region of interest.

Three cases are shown throughout this work: one without an airfoil, one with the NACA 0008, and one with the NACA 0018. The simulation without the airfoil was performed to mirror the experimental approach, where the turbulence was characterized with an empty test section[23] before studying the effects of the presence of the airfoil.[24] The number of cells in the domain was 300×10^6. The simulations were run for 2 s of physical time (over 160 flow passes, based on c), with the first 0.2 s being dismissed as the initial transient. The flow coming from the inlet takes about 0.07 s to reach the airfoil, meaning the flow goes over the airfoil for about 0.13 s (11 flow passes) during the initial transient. This initial transient was selected based on the convergence of the mean velocity toward a constant value at the target airfoil LE location by taking windows of 0.1 s. The simulation duration was chosen based on the statistical convergence of the mean and root mean square (RMS) of the velocity fluctuations, turbulence spectrum, turbulence length scale, wall pressure spectrum on the airfoil LE region, and far-field noise. Out of these quantities, the turbulence length scale seems to be the most sensitive to the simulation duration. While other quantities showed small variations by comparing the signal for 0.2–1.2 s to 0.2–2.0 s, the length scale for the empty tunnel case near the target

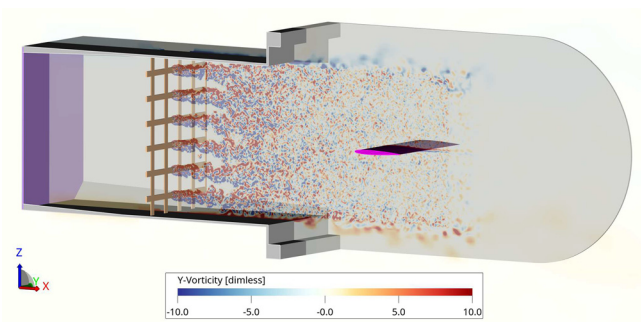

FIG. 3. Slice showing spanwise vorticity, along with the open test section. The sidewall closer to the viewer's side is hidden for clarity.

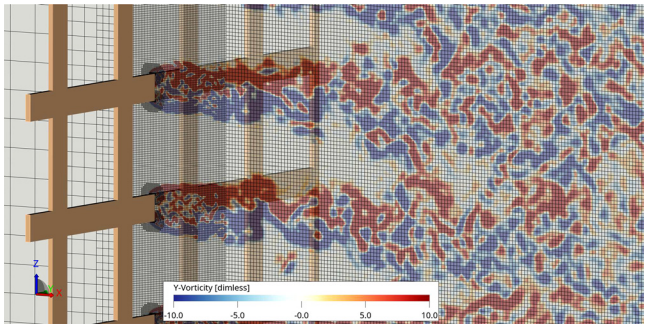

FIG. 4. Computational mesh near the turbulence grid. Every second mesh line is shown for clarity.

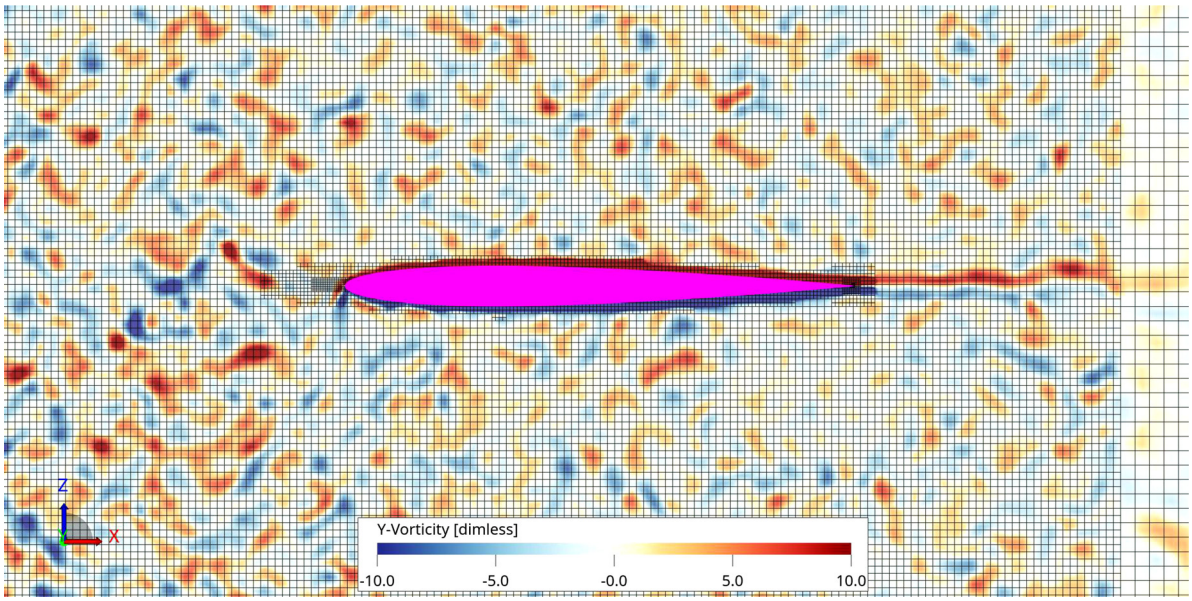

FIG. 5. Computational mesh near the airfoil. Every second mesh line is shown for clarity.

airfoil LE at various values of z had a scatter of over 14 mm for the shorter run time and 8 mm for the longer run time, corresponding to 35% and 20% of the mean, respectively. This is associated with the uncertainties in calculating the length scale, which will be covered in Sec. V B. While a longer run time would further reduce this uncertainty, we chose 2 s as the total run time because the far-field noise was unaffected. Simulations took about 50 000 central processing unit (CPU) h on 280 cores, which corresponds to about one week of wall-clock time.

C. Mesh resolution effects

A concise mesh resolution study is discussed in this section to verify the consistency of the numerical results. This study is performed by coarsening the mesh for the case with the NACA 0008 airfoil by a linear factor of 1.25, meaning that number of cells is almost halved for the coarse case, and verifying the comparability of the velocity and WPF spectra for the cases of fine and coarse meshes.

The analysis starts by verifying whether the mesh affects the freestream turbulence, which is shown in Fig. 6. The power spectral density (PSD) of the streamwise and transverse velocity components at $x = -30r_{LE}$, i.e., in the freestream, is measured for the coarse and fine meshes. In this paper, the PSD of the velocity components (Φ_{uu} and Φ_{ww}), WPF (G_{qq}), and far-field pressure fluctuations (G_{pp}) are estimated using Welch's method.[68] The spectral level is shown in decibels, where the reference values were 1 m/s for Φ_{uu} and Φ_{ww}, and 20 μPa for G_{qq} and G_{pp}. Hanning windows were used, with an overlap of 50%. The results shown in Fig. 6 match well for $f < 1000$ Hz, with the only notable difference being the numerical cutoff of the coarse mesh appearing earlier, as expected. In Sec. V A, it is shown that the cutoff frequency for the simulation is at approximately 2 kHz.

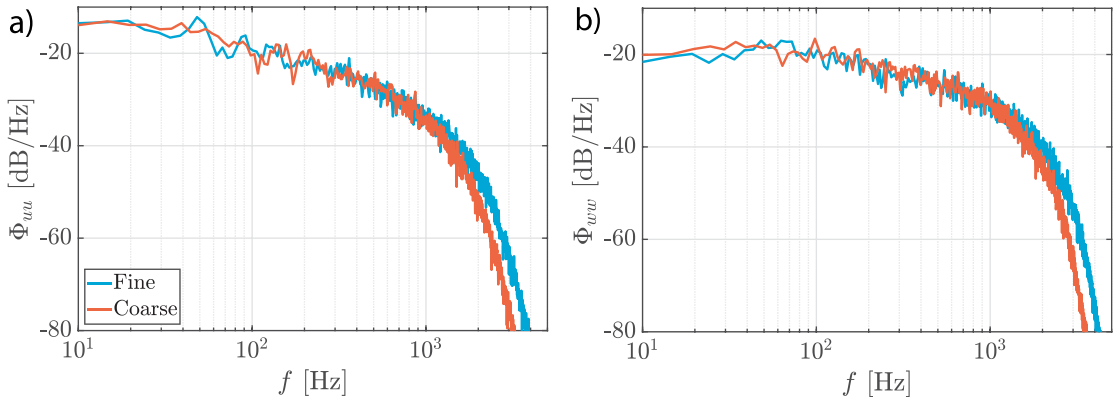

FIG. 6. PSD of the streamwise (a) and transverse (b) velocities at $x = -30r_{LE}$ for the case with the NACA 0008 airfoil for simulations with a fine and a coarse mesh (number of cells almost halved).

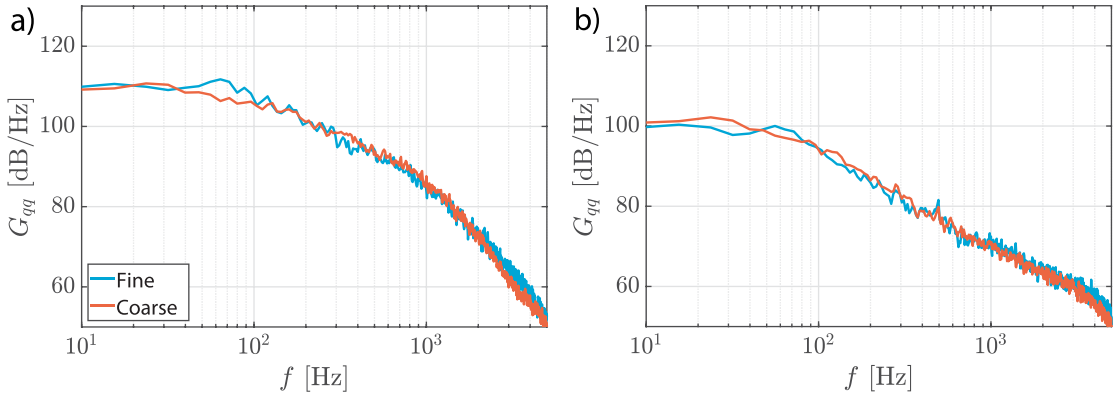

FIG. 7. PSD of the WPF on the NACA 0008 surface at $x/c = 0.0035$ (a) and $x/c = 0.1$ (b) for simulations with a fine and a coarse mesh (number of cells almost halved).

Next, the WPF spectra for the two meshes are compared, which is an indicator of the sensitivity of the mesh near the airfoil. Results are shown in Fig. 7. Some minor differences of up to $2-3$ dB are seen around 70 Hz for $x/c = 0.0035$, which correspond to the small differences seen in Fig. 6 for the same frequency range. For the other frequencies, the results overlap, which is not entirely expected. As the coarse mesh has a noticeable earlier cutoff near 1500 Hz, one could expect the results above this frequency to be very different for the two meshes and to decay quickly toward zero. However, the high frequencies of the WPF spectrum do not seem to correspond directly to the high frequencies of the velocity spectrum in the freestream spectrum because the level of Φ_{uu} is effectively zero at 5000 Hz [Fig. 6(a)]. This will be discussed further in Sec. V F.

The differences shown in Figs. 6 and 7 are considered to be acceptable. Thus, the results from this study are considered to be grid converged up to nearly 2000 Hz.

V. RESULTS

A. Validation of the freestream turbulence simulation with no airfoil

This section compares the numerical results to the experimental data available in the literature[23] for the grid-generated turbulence without the airfoil present in the test section.

The numerical and experimental spectra of the streamwise velocity u and the transverse velocity w are shown in Fig. 8. The von Kármán turbulence spectrum is also included in these figures because this formulation is often used as input for LE noise calculations and is representative of isotropic turbulence. These spectra are determined at $x = 0$, which is the location where the airfoil LE would be. The level and frequency of the experimental spectrum are scaled to consider the minor differences in mean velocity between the experimental and numerical results. The frequency f is scaled as the Strouhal number based on Λ_f and $\bar{u}$. The spectral level of Φ_{uu} (or Φ_{ww}) is scaled by analyzing Eqs. (4), (5), and (8). The final scaling for the frequency and level of the experimental spectrum is

$$f_{\text{Exp.,scaled}} = f_{\text{Exp.}} \frac{\bar{u}_{\text{Num.}}}{\bar{u}_{\text{Exp.}}} \frac{\Lambda_{f\,\text{Exp.}}}{\Lambda_{f\text{Num.}}}, \tag{9}$$

$$\Phi_{\text{Exp.,scaled}} = \Phi_{\text{Exp.}} \frac{\bar{u}_{\text{Exp.}}}{\bar{u}_{\text{Num.}}} \frac{\Lambda_{f\text{Num.}}}{\Lambda_{f\,\text{Exp.}}} \frac{u^2_{\text{rms,Num.}}}{u^2_{\text{rms, Exp.}}}. \tag{10}$$

The streamwise experimental spectrum (Φ_{uu}) matches the von Kármán spectrum well in the entire frequency range, whereas the streamwise numerical spectrum slightly overpredicts the energy levels for $300 < f < 2000$ Hz; see Fig. 8(a). For the transverse velocity spectrum (Φ_{ww}), both experimental and numerical spectra have higher

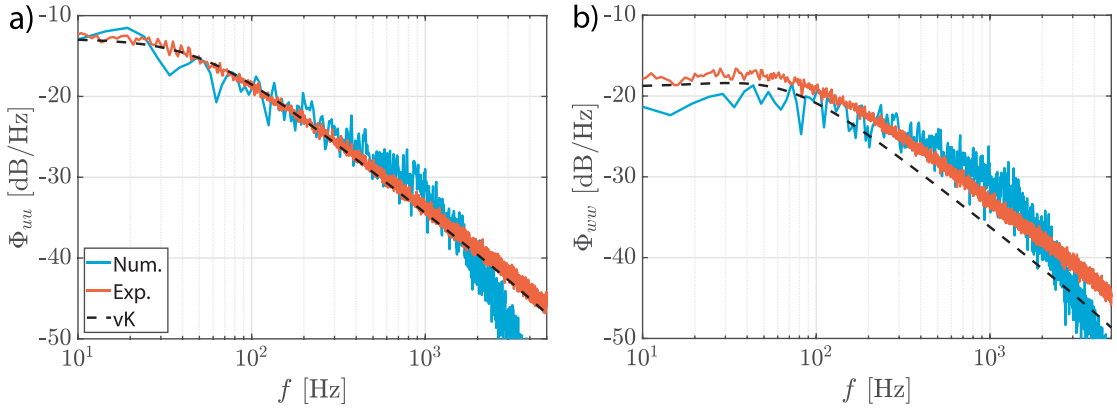

FIG. 8. PSD of the streamwise (a) and transverse (b) velocities at $x = 0$ (target LE location) for the case without the airfoil. Num.—numerical results, Exp.—experimental results,[23] vK—von Kármán spectrum.

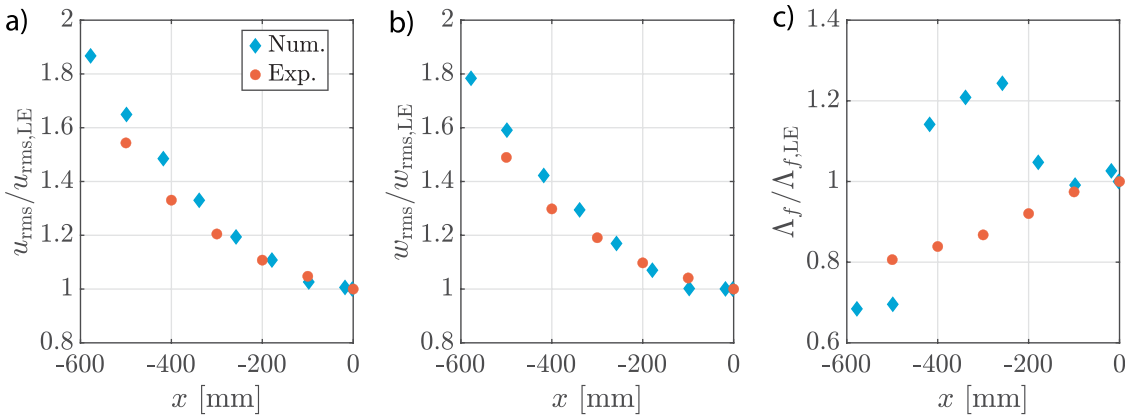

FIG. 9. RMS of the velocity fluctuations and longitudinal length scale at mid-span and $z = 0$ along the streamwise direction. Num.—numerical results, Exp.—experimental results.[23]

spectral levels than predicted by the von Kármán turbulence spectrum; see Fig. 8(b). The von Kármán model was developed for an isotropic turbulent flow; thus, the difference between the experimental/numerical spectra with the von Kármán spectrum for the transverse velocity indicates some level of anisotropy in the turbulence. As observed for Φ_{uu}, the numerical spectrum Φ_{ww} has higher energy levels than the experimental one for $300 < f < 2000$ Hz. The numerical spectra (Φ_{uu} and Φ_{ww}) decay rapidly for frequencies above 2 kHz, which is the numerical cutoff of the simulations. In general, a reasonable agreement between the numerical, experimental, and von Kármán spectra is observed for frequencies up to 2 kHz.

Figure 9 compares the numerical and experimental results of the RMS of the streamwise and transverse velocity fluctuations and the longitudinal length scale along the streamwise direction at mid-span and $z = 0$. These quantities are normalized by the values extracted at the LE location without the airfoil, i.e., $u_{RMS,LE}$, $w_{RMS,LE}$, and $\Lambda_{f,LE}$. The numerical results for the RMS of the velocity fluctuations follow a similar decay as the experimental results; see Figs. 9(a) and 9(b). The numerical integral length scale has a similar tendency as the experimental length scale for $-100 < x < 0$; see Fig. 9(c). However, a significant discrepancy is observed for $-400 < x < -200$ mm. Section V B discusses the reason for this mismatch. We conclude from comparing the numerical and experimental results that the numerical turbulence presents similar trends as the experimental turbulence, except for the integral length scale.

B. Integral length scale determination

The longitudinal integral length scale Λ_f is a statistical parameter that quantifies the streamwise dimension of the largest turbulent structures present in the turbulent flow. This parameter is computed following the method proposed by Hinze.[69] This method was also used by dos Santos *et al.*[23] to compute the integral length scale from hot-wire measurements, which are used to validate the numerical results. In this method, the turbulence timescale is determined as the time when the autocorrelation of the streamwise velocity reaches zero for the first time. In light of Taylor's frozen turbulence hypothesis,[70] the longitudinal integral length scale is computed considering that the turbulence is convected with the mean flow velocity at the measurement location, which, according to Pope,[71] provides accurate results. According to Lin,[72] this hypothesis is valid when $u^2_{rms} \ll \bar{u}^2$. For the results discussed in this paper, u^2_{rms} was two orders of magnitude smaller than $\bar{u}^2$, making this hypothesis valid.

In Fig. 9(c), the abrupt increase and decrease in the integral length at $x = -258$ mm and $x = -418$ mm, respectively, are attributed to the method used to determine the integral length scale. To clarify this, the autocorrelation of the streamwise velocity is analyzed for the locations $x = -498$ mm and $x = -418$ mm; see Fig. 10. The autocorrelation for $x = -418$ mm oscillates close to zero but does not cross zero as quickly as the autocorrelation for $x = -498$ mm. Thus, the timescale determined from the first-zero crossing for $x = -418$ mm is longer than the timescale at $x = -498$ mm, resulting in a larger integral length scale for $x = -418$ mm. The autocorrelations for the numerical data for $-100 < x < 0$ mm and $-600 < x < -498$ mm present the oscillatory behavior close to zero to a much lesser extent than the data for $-418 < x < -258$ mm, showing a better agreement with the experiments; see Fig. 9(c). The experimental integral length scale in Fig. 9(c) continuously increases with the streamwise position, indicating that

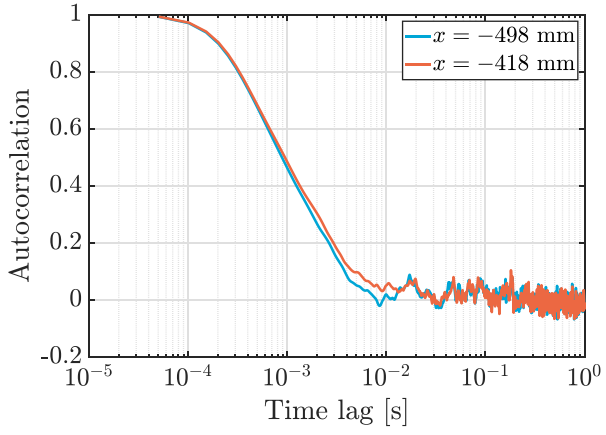

FIG. 10. Autocorrelation of the numerical streamwise velocity fluctuations at two streamwise positions at mid-span and $z = 0$.

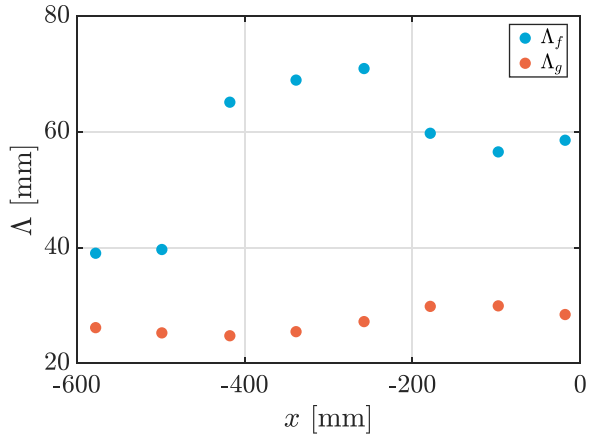

FIG. 11. Streamwise and z-direction integral length scales. Numerical data.

the numerical results are likely more susceptible to this effect because the numerical data were obtained for a relatively shorter time (2 s signal length) than the experimental data (30 s signal length). Thus, the numerical values for Λ_f should be considered with a substantial margin of uncertainty. There are other methods to determine the integral length scale, e.g., by fitting an exponential curve to the autocorrelation data, by considering the timescale as the time period needed for the autocorrelation to decrease to $1/e$,[73] or by integrating the correlation of streamwise velocity in the streamwise direction.[71] These methods were analyzed in this research. However, these approaches also did not result in consistent values and tendencies of the longitudinal integral length scale for all data points used. Thus, we decided to compute the integral length scale based on the traditional calculation method proposed by Hinze.[69]

Figure 11 shows the streamwise and transverse (Λ_g) integral length scales for the simulations. The transverse integral length scale is calculated by integrating the correlation of the transverse velocity in the z-direction, as discussed by Pope.[71] Experimental results for the transverse integral length scale with the streamwise position are not available. For isotropic turbulence, it is expected that $\Lambda_f \approx \Lambda_g$. Figure 11 shows that the turbulence generated numerically results in $\Lambda_f \approx 2\Lambda_g$ at the LE, indicating that the turbulence is not isotropic at the LE, confirming what is discussed in relation to Figs. 8(a) and 8(b). Petrikat *et al.*[33] performed LES simulations of a grid-generating turbulence. They observed that the grid-generated turbulence resulted in $\Lambda_f \approx 2\Lambda_g$, which agrees with the results of the current study at the LE location.

C. Influence of airfoil on the inflow turbulence

This section investigates the turbulence distortion due to the presence of the airfoil. First, the numerical results are compared with the available experimental data.[24] Subsequently, the numerical results of the turbulence in the vicinity of the airfoils are analyzed in detail.

Figure 12 shows the numerical and experimental results of mean streamwise velocity $\bar{u}$, RMS of the streamwise velocity fluctuations u_{rms}, and integral length scale Λ_f along the stagnation line of the NACA 0008 airfoil. These values are normalized by their freestream quantities, which are extracted at $x/r_{\text{LE}} = -30$, because the experiments were conducted at a slightly different freestream velocity as the velocity used in the simulation (26.5 m/s in experiments and 25 m/s in simulations). The streamwise distance x is normalized with the LE radius of the airfoil. Figure 12(a) shows the decay of $\bar{u}$ as the stagnation point is approached, resulting in a zero velocity at the stagnation point, as expected. A good agreement between the simulation and the experimental data is observed for the mean velocity. Figure 12(b) shows that the experimental u_{rms} reasonably agrees with the simulation results. The experimental u_{rms} values slightly increase for $x/r_{\text{LE}} > -1$, which likely occurs because the hot-wire probe used to perform the measurements was not precisely at the stagnation line. Figure 12(c) shows a good agreement between the numerical and experimental integral length scales. It is important to mention that the behavior of the autocorrelation discussed in Sec. V B is not observed for the results shown in Fig. 12(c). This means that the autocorrelation for the streamwise positions shown in Fig. 12(c) crossed zero quickly, resulting in a smooth decay of the integral length scale as the LE position is approached. The integral length scale was computed using different methods, as discussed in Sec. V B, presenting the same trend observed in Fig. 12(c). Therefore, the results in Fig. 12 indicate that the

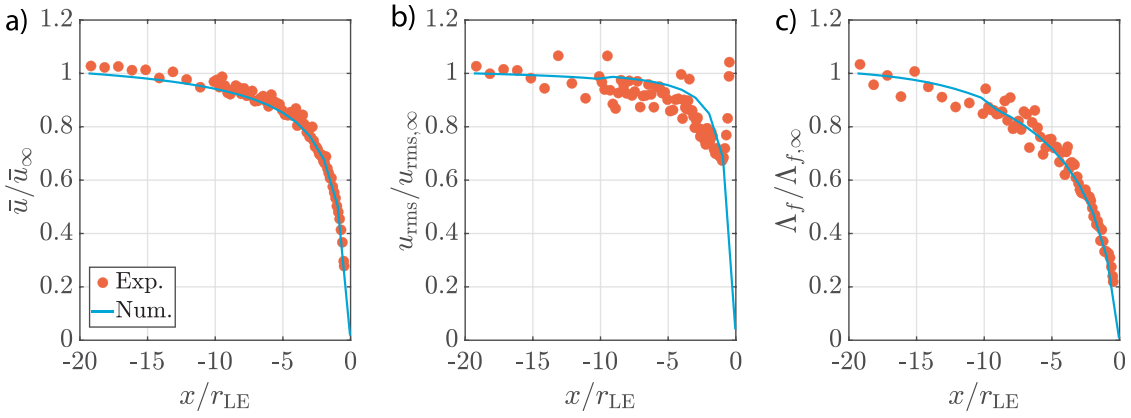

FIG. 12. Flow quantities at the stagnation line of the NACA 0008 airfoil at mid-span. Average streamwise velocity (a), RMS of the streamwise velocity fluctuations (b), and longitudinal integral length scale (c). Num.—numerical results, Exp.—experimental results.[24]

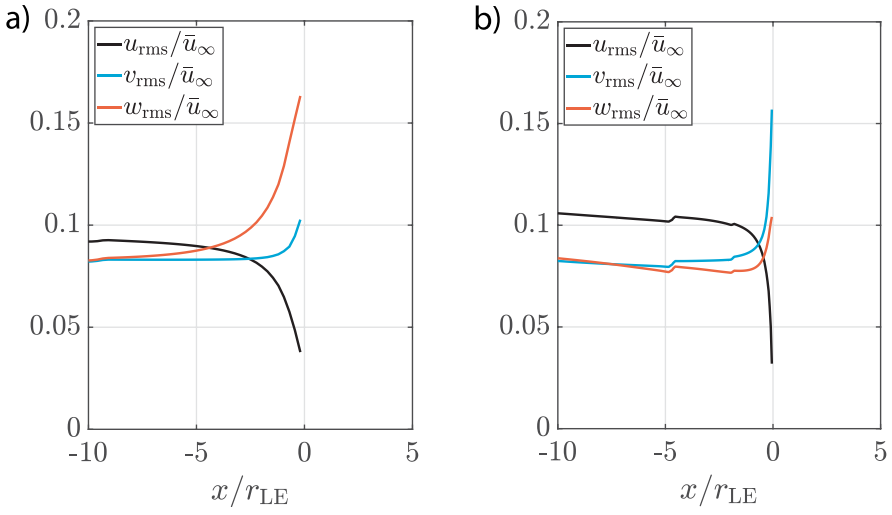

FIG. 13. Numerical results of the turbulence intensity of the three velocity components at mid-span along the stagnation streamline for the NACA 0008 (a) and NACA 0018 (b) airfoils.

simulated flow near the LE agrees with the experimental observations well. As the experimental data are limited in proximity to the airfoil LE due to the difficulty in performing these measurements, the numerical data can give new insight into the turbulence distortion phenomenon for airfoils.

Figure 13(a) shows the numerical results of RMS values of the streamwise, spanwise, and transverse velocity components (u, v, and w, respectively) at the NACA 0008 stagnation streamline. We observe that u_{rms} tends to zero but does not reach it at the wall due to the sampling being off-body, the coarse mesh on the boundary layer, and the use of wall functions. The component associated with LE noise, w_{rms}, increases substantially near the LE. The spanwise component v_{rms} is less affected by the NACA 0008 airfoil. The changes in the RMS quantities for Fig. 13(b) near $x/r_{\mathrm{LE}} = -5$ and -2 are due to jumps in resolution of the Cartesian grid, which allow for higher frequencies to be resolved, particularly in an ILES scheme. They do not appear in Fig. 13(a) because they are outside the range of the figure due to the normalization of the x axis by the r_{LE}.

We perform the same analysis for the NACA 0018 airfoil in Fig. 13(b). Note that scaling the x axis with r_{LE} does not lead to similar curves for both airfoils, which fact we will address later in this work. Although the trends of the streamwise velocity fluctuations for the NACA 0018 are to a certain extent similar to the NACA 0008 results, noticeable differences are seen for the v_{rms} and w_{rms} results. Contrary to the results for the NACA 0008, the spanwise turbulence intensity for the NACA 0018 increases near the LE more considerably than the transverse velocity.

To understand the different trends in spanwise and transverse velocities near the LE of the NACA 0008 and NACA 0018, the transverse (z-direction) vorticity is analyzed. Figure 14 shows the transverse vorticity in the range $\pm 15\bar{u}_\infty/c$ for the NACA 0008 and NACA 0018. The thicker airfoil leads to vortical structures that wraparound the LE, distorting the incoming turbulence and accumulating transverse vortices in front of the LE. In LE noise theory, the transverse flow fluctuations associated with spanwise vortices are the main noise source for LE noise.[63] Figure 14 shows that for a thicker airfoil, spanwise flow fluctuations associated with transverse vortices dominate the flow near the LE and just upstream of it. This figure shows an arbitrary spanwise location where the accumulation of transverse vortices happens for both airfoils. However, the vortices upstream of the NACA 0018 LE are larger and stronger. In addition, we observed that such behavior is very common along the span of the NACA 0018 and is fairly rare along the span of the NACA 0008.

The vortices in the transverse direction that impinge on the airfoil LE and wraparound it are difficult to visualize in three dimensions in the fluid due to the background turbulence. Typical isosurfaces that are often used to visualize vortices of high-fidelity simulations[74] do not allow us to isolate vortices close to the surface easily and that bend, changing from having transverse to streamwise vorticity. Hence, it is more practical to visualize these vortices indirectly by analyzing their footprint on the airfoil surface. This is done in Fig. 15, where the spanwise surface skin friction is shown in the range $\pm 0.002 q_\infty$, where q_∞ is the freestream dynamic pressure. The red and blue streaks correspond to positive and negative forces, respectively. We can see stronger spanwise forces acting on the LE region of the NACA 0018 airfoil compared to the NACA 0008. The red and blue streaks running from the LE up to about 30% of the chord are due to the vortices wrapping around the NACA 0018 LE. This occurs with a lower intensity and on a smaller extension of the chord length for the NACA 0008. This is likely associated with the NACA 0008 sharper LE, which splits the incoming vortices due to the smaller stagnation region.

According to the RDT for cylinders, the turbulence distortion effects depend on the ratio Λ_f/r, where r is the cylinder radius.[20,21] Considering the LE radius as characteristic length, this ratio is $\Lambda_f/r_{\mathrm{LE}} = 27.2$ for the NACA 0008 and $\Lambda_f/r_{\mathrm{LE}} = 5.3$ for the NACA 0018, where the Λ_f is considered as the value at the LE without the airfoil. The results in the stagnation line for the NACA 0008 [Fig. 13(a)] are consistent with the RDT calculations for $\Lambda_f \gg r$:[20,21] u_{rms} decreases as the stagnation point is approached because of the blockage imposed by the airfoil, whereas w_{rms} increases due to the momentum transfer. Meanwhile, v_{rms} is not expected to change according to the RDT. Even though this component remains mostly constant in the stagnation line of the NACA 0008, it slightly increases close to the airfoil LE. These results show that the turbulence distortion mechanism observed for a cylinder for $\Lambda_f \gg r$ is also observed for an airfoil when this ratio is respected. For the NACA 0018, the trend expected from

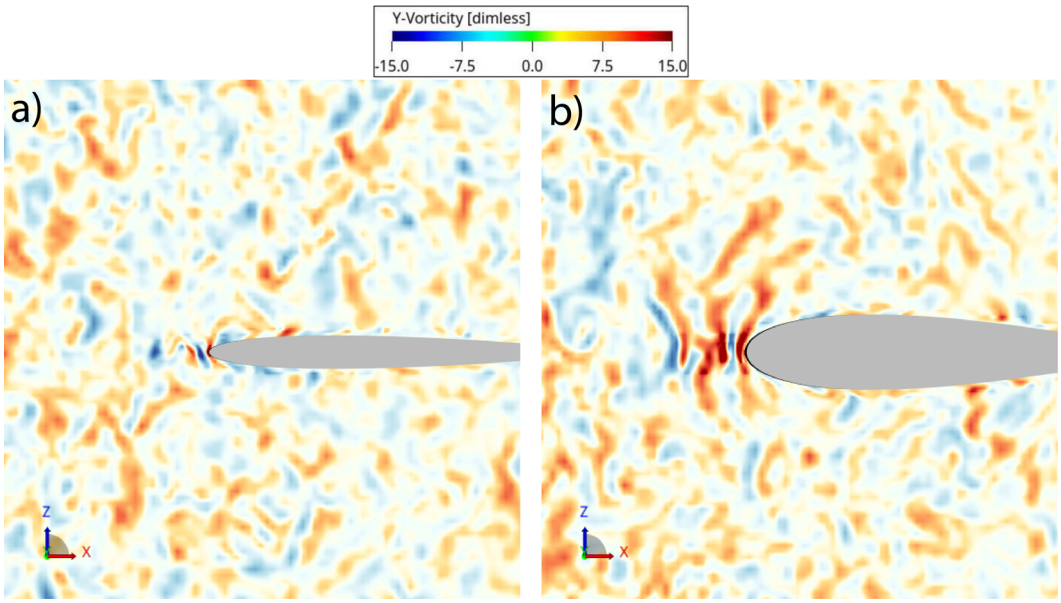

FIG. 14. Slice in the *x*-*z* plane of the instantaneous transverse vorticity near the LE of the NACA 0008 (a) and NACA 0018 (b). Numerical data.

the RDT asymptotic results is also observed but to a lesser degree: the transverse velocity fluctuations increase as the LE is approached, whereas the spanwise component increases comparatively more; see Fig. 13(b). This change in trend occurs because the NACA 0018 LE radius is more comparable to the integral length scale, where the RDT asymptotic results for $\Lambda_f \gg r$ start to be invalid. Thus, the turbulence distortion mechanism observed for the NACA 0018 is different than that for the NACA 0008.

Figure 16 shows the streamwise, transverse, and spanwise spectra at streamwise positions along the stagnation line of the NACA 0008 airfoil. The spectral level of Φ_{uu} decreases as the stagnation point is approached, whereas the level of Φ_{ww} increases, especially for frequencies below 200 Hz. Higher frequencies seem less affected by the presence of the airfoil. The levels for Φ_{vv} show very little change, as expected, since the main momentum transfer occurs between the streamwise and transverse velocity components. The level decrease in Φ_{uu} and the level increase in Φ_{ww} confirm the momentum transfer from the streamwise component to the transverse component, which is responsible for the turbulence distortion, agreeing with the previous discussion. These results also show that the momentum transfer is concentrated in the large turbulence scales, i.e., low frequencies. The medium-length scales, i.e., mid-frequency range, are mainly unaffected by the turbulence distortion. According to the energy cascade theory and the Kolmogorov hypotheses, the outer flow parameters, i.e., mean flow field and pressure gradient, affect only the large scales and, as the energy is transferred from the large to the small scales, all the information about the geometry of the large scales, i.e., mean flow field and boundary conditions, is lost.[71] This observation suggests that the mean flow does not affect the mid-frequency range. Additionally, Gill *et al.*[12] attribute the turbulence distortion in the stagnation region of an airfoil

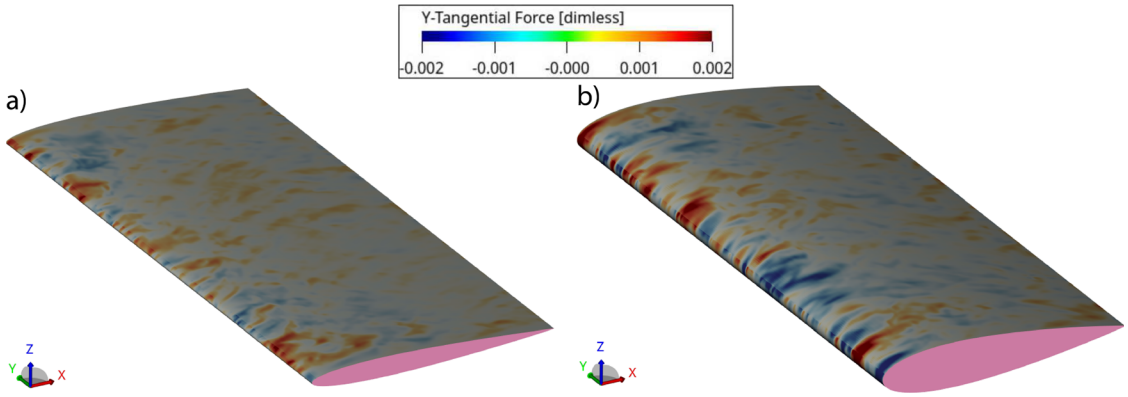

FIG. 15. Instantaneous spanwise skin friction for the NACA 0008 (a) and NACA 0018 (b). Numerical data.

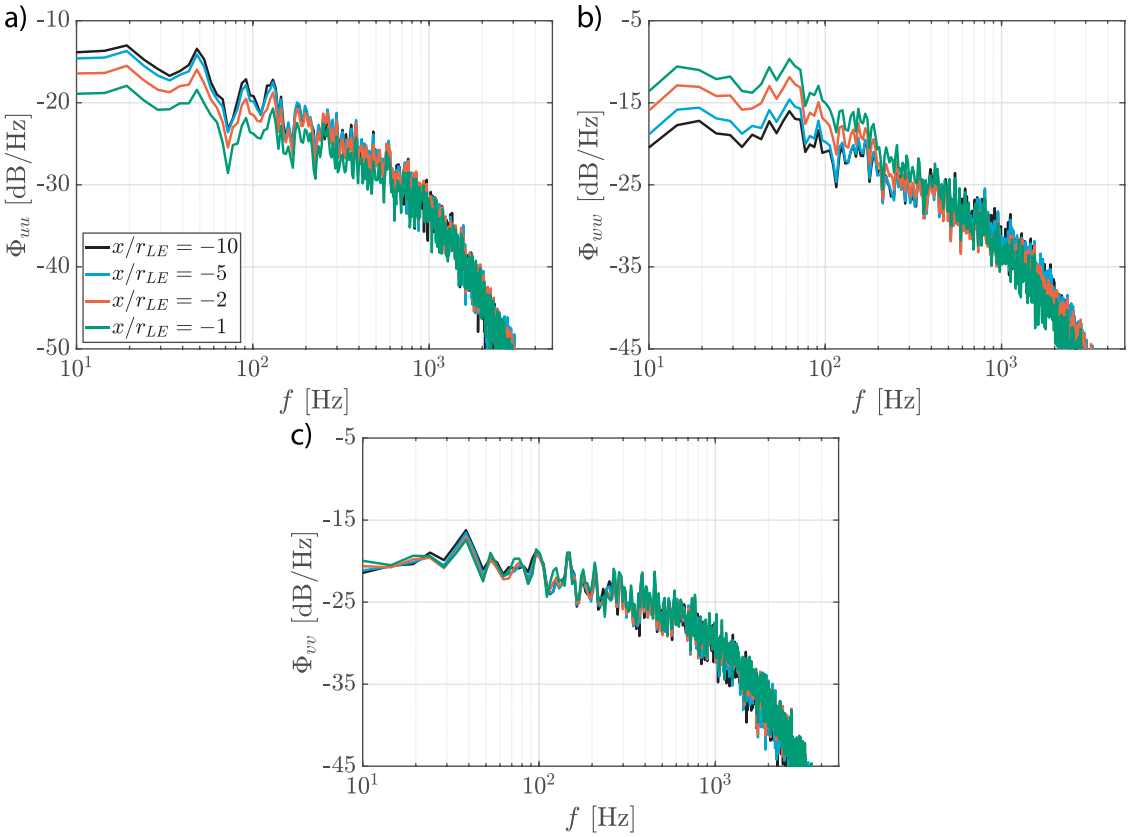

FIG. 16. PSD of the numerical streamwise (a), transverse (b), and spanwise (c) velocity fluctuations along the stagnation line of the NACA 0008 at mid-span.

to the velocity gradients present in this region. Thus, it is reasonable that the mid-frequency range is not affected by the turbulence distortion because the mean flow field does not impact this frequency range. Furthermore, the effect of the turbulence distortion for frequencies higher than 2 kHz cannot be analyzed because this is the cutoff frequency of the simulation. Similar tendencies for the velocity spectra are observed for the NACA 0018, which correspond to the tendencies presented in Fig. 13(b). Hence, the corresponding graphs are omitted here for brevity.

Next, the scaling of the main flow quantities in the stagnation line with airfoil geometrical parameters is investigated. Figure 17(a) shows the mean streamwise velocity at the stagnation line with the streamwise position scaled with the airfoil maximum thickness. $\Delta\bar{u}$ is the difference between the mean streamwise velocity for the cases with and without the airfoils. We scaled the vertical axis to achieve values between zero and unity. The best scaling of the mean velocity is obtained when the horizontal axis is normalized by the airfoil maximum thickness $t_{\max}$. According to Gill *et al.*,[12] the turbulent inflow is distorted due to a pressure gradient in the stagnation area, which depends on the airfoil geometry in the LE region. As the airfoil maximum thickness is the largest dimension blocking the flow field, resulting in the stagnation region, it is reasonable that the velocity scales with this dimension. The scaling of Λ_f is shown in Fig. 17(b), where the curves for both airfoils overlap when the streamwise coordinate is scaled by the airfoil LE radius r_{LE}. The integral length scale curves are smoothed to avoid the discontinuities in Λ_f for the case of the NACA 0018, as those seen in Fig. 11, which introduces a certain degree of uncertainty regarding the scaling. The vertical axis is scaled to result in values between zero and unity, which is done by using $\Delta\Lambda_f$, i.e., the difference between Λ_f for the cases with and without the airfoils, adding $\Lambda_{f,0}$, which is Λ_f at $x = 0$ for the case without the airfoils, and dividing each curve by a reference value taken arbitrary at $x/r_{\mathrm{LE}} = -10$. Figure 17(c) shows the u_{rms} values at the stagnation line of the airfoils. Contrary to the mean velocity and length scale, the u_{rms} curves do not require any scaling of the streamwise coordinate to collapse. The vertical axis is scaled with the value of u_{rms} at the arbitrary reference point of -6 mm. Similar behavior is observed for w_{rms}; see Fig. 17(d). For this case, the vertical axis is scaled with the value of w_{rms} at the arbitrary reference point of $x = -10.5$ mm and the maximum value of w_{rms} since $w_{\mathrm{rms,max}}$ changes considerably from one airfoil to the other. Note that the location of maximum thickness for both airfoils is at the same chordwise position; hence, it is possible that u_{rms} scales with x/x_{tmax} or x/c. Finally, Fig. 17(e) shows the v_{rms} scaling, which seems to scale with x/r_{LE}. The reference location used to normalize v_{rms} is $x/r_{\mathrm{LE}} = -4$, as this quantity seems to start changing dramatically only very close to the LE. For the NACA 0008 airfoil, more points are likely needed to capture the peak value of v_{rms}, but both airfoils show a strong growth in v_{rms} around $x/r_{\mathrm{LE}} = -2$ and,

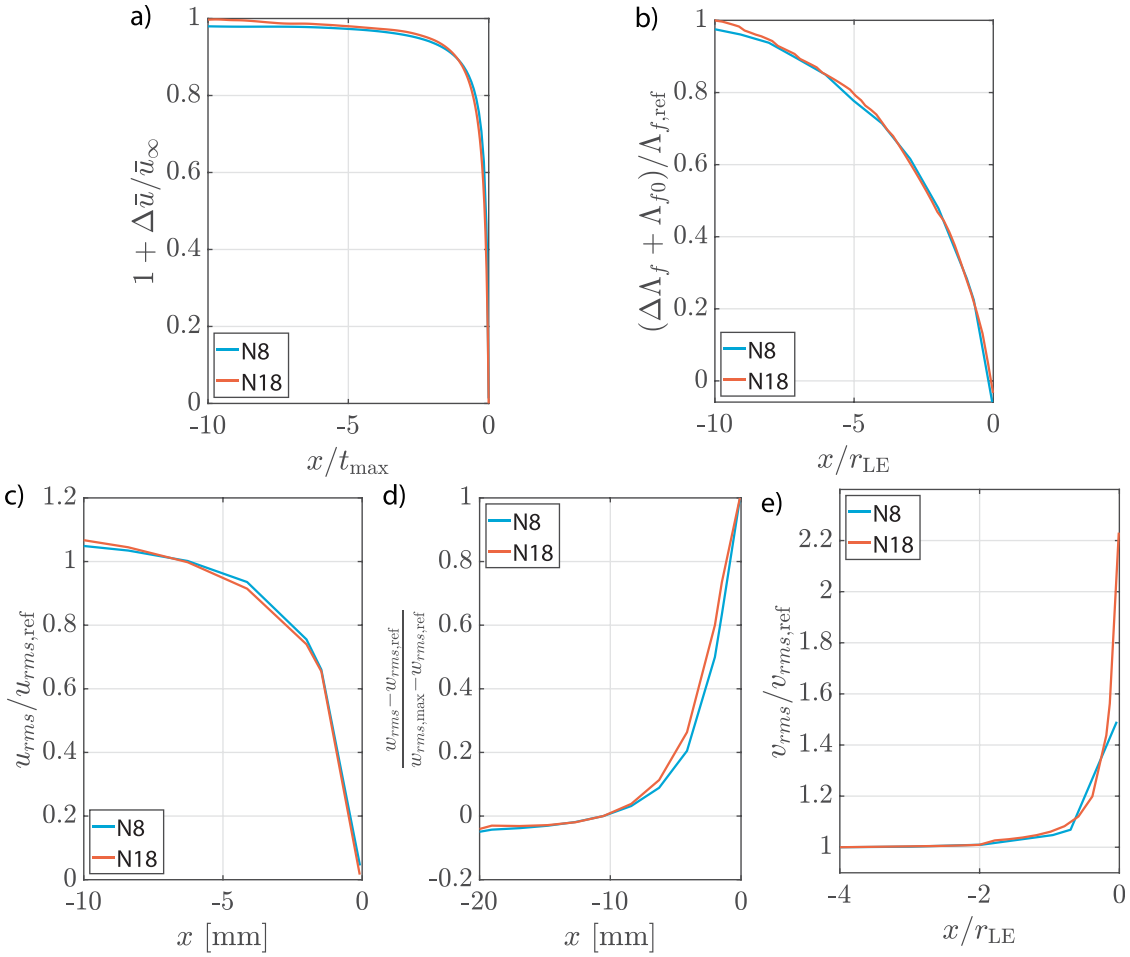

FIG. 17. Flow quantities at the stagnation line of the airfoils at mid-span normalized by different parameters. Average velocity (a), integral length scale (b), RMS of the streamwise (c), transverse (d), and spanwise (e) velocity fluctuations. Numerical data.

initially, the growth rates seem comparable. Figure 17 shows that different flow quantities scale differently near the stagnation point, with the results for u_{rms} and Λ_f being particularly important for noise predictions using the RDT-based turbulence spectrum since the main inputs for this formulation are u_{rms} and Λ_f near the LE.

D. Wall pressure spectra

We evaluate the behavior of the WPF near the NACA 0008 LE in Fig. 18. Six curves are shown: the experimental measurements ("Exp."), the numerical results ("Num."), the Amiet prediction using the von Kármán spectrum with input $\bar{u}$, u_{rms}, and Λ_f from either the experiments ["Amiet(vK)-Exp."] or the simulations ["Amiet(vK)-Num."] extracted at the LE location without the airfoil, and the Amiet prediction using the RDT spectrum with input the $\bar{u}$, u_{rms}, and Λ_f from either the experiments ["Amiet(RDT)-Exp."] or the simulations ["Amiet(RDT)-Num."] extracted at the LE location without the airfoil. At $x/c = 0.0035$, in Fig. 18(a), we observe a near constant shift of about 10 dB between Amiet(vK)-Num. and the numerical spectrum for frequencies below 30 Hz, whereas the experimental data are close to the numerical results. Between 300 and 1000 Hz, the Amiet(vK) predicts WPF spectral levels between the numerical and experimental levels. The experimental spectrum at $x/c = 0.0035$ is less reliable than at positions further downstream due to the difficulty of calibrating the microphones because of the high curvature of the airfoil LE at this position. Amiet(RDT) does not approximate the numerical and experimental spectra. However, the decay observed for the numerical spectrum for $f > 1$ kHz is similar to that of the Amiet(RDT)-Num. This frequency range is close to the simulation cutoff frequency; therefore, these results may not be reliable. Similar results are observed for the NACA 0018; hence, results for this geometry are omitted for brevity. The WPFs at this chordwise position, i.e., $x/c = 0.0035$, are due to the direct impingement of the turbulent inflow on the surface because the boundary layer is barely developed yet.

In Fig. 18(b), at $x/c = 0.10$, the discrepancies between numerical, experimental, and Amiet(vK) spectra are smaller than at $x/c = 0.0035$. We observe a near-constant shift between the numerical and experimental spectra, which is expected because of a slight difference in freestream velocity for these cases. This shift is comparable to the corresponding differences between the Amiet curves

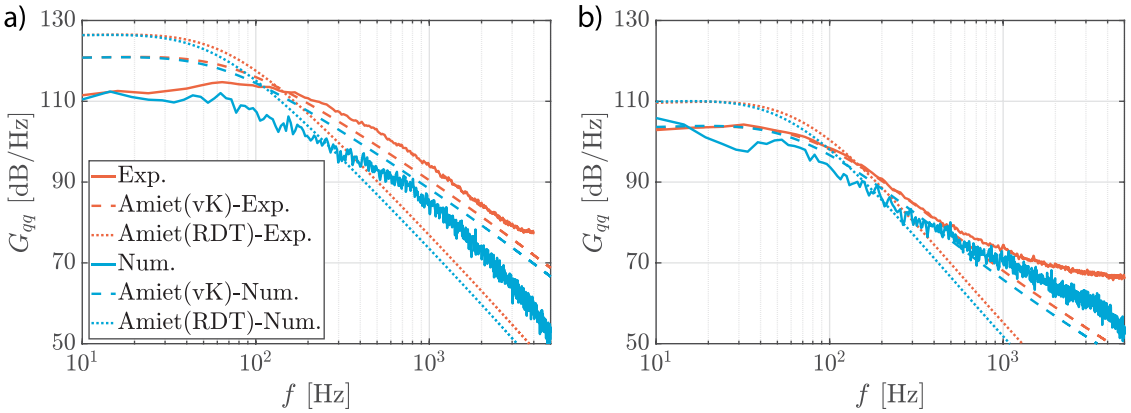

FIG. 18. PSD of the WPF on the NACA 0008 surface at $x/c = 0.0035$ (a) and $x/c = 0.10$ (b) at mid-span. Num.—numerical results, Exp.—experimental results,[24] Amiet prediction—Eq. (2).

Amiet(vK)-Exp. and Amiet(vK)-Num. The Amiet prediction Amiet (vK) agrees with the experimental and numerical spectra reasonably well up to 500 Hz. For frequencies above approximately 500 Hz, the experimental spectrum changes slope, which is attributed to the boundary layer influence on the WPF. The simulation does not capture this, as the coarsely resolved, wall-modeled flow does not resolve the small fluctuations inside the boundary layer. According to previous research,[75,76] the freestream turbulence penetrates the boundary layer when the turbulence length scale of the free stream is significantly larger than the length scale in the boundary layer. This phenomenon influences the length scales in the boundary layer differently. Dogan *et al.*[75] showed that the freestream turbulence penetrates the outer part of the boundary layer, and for sufficiently high turbulence levels, it can penetrate up to locations very close to the wall, i.e., up to the small scales, resulting in a modulation of these scales. The results in Fig. 18(b) indicate that the freestream turbulence penetrates the boundary layer and induces the pressure fluctuations for $f < 500$ Hz. This is stated for two reasons. First, the Amiet theory only considers the impingement of the turbulent inflow on the surface, not accounting for the boundary layer development, and there is a good agreement between the Amiet prediction Amiet(vK) and the numerical and experimental spectral curves for $f < 500$ Hz. Second, the spectral decay at $x/c = 0.10$ in the range $100 < f < 500$ Hz for both numerical and experimental spectra follows a similar decay as that at $x/c = 0.0035$ in the range $200 < f < 1000$ Hz for the numerical data and $200 < f < 3000$ Hz for the experimental data, which is due to the direct impingement of the turbulent inflow. For $f > 500$ Hz, the WPF spectral levels are associated with the boundary layer because the penetration of the freestream turbulence is more difficult to occur for the smaller length scales in the boundary layer, and it only causes a modulation of these scales.[75] Furthermore, the Amiet(vK) curves are much closer to the corresponding experimental and numerical spectra than the Amiet(RDT) data for $f > 500$ Hz, indicating that the turbulence distortion effect does not play a major role downstream from the LE, with the WPF at this location being mostly affected by the freestream turbulence and the boundary layer development. As we will see later in Sec. V E, $x/c = 0.0035$ is a region of very high gradients of the pressure fluctuations, while $x/c = 0.10$ has a less steep gradient. Hence, small differences in probe placement or turbulence decay can lead to larger errors closer to the LE. This justifies the larger discrepancies between experimental and numerical spectra at $x/c = 0.0035$.

Considering that the larger discrepancy between the Amiet(vK) prediction and the simulation/experiment at $x/c = 0.0035$ is related to the turbulence distortion effects, which are mostly concentrated in the LE region, the prediction of the WPF might be improved by using the distorted turbulence parameters as input to the Amiet prediction. As discussed in Sec. V C, the turbulence parameters used as input to the Amiet model change considerably in the LE vicinity. Hence, we verify the behavior of the WPF prediction considering as input the turbulence parameters extracted close to the LE, i.e., the distorted turbulence parameters. We extract the turbulence input parameters at the stagnation line at $x/r_{LE} = -2$ for the NACA 0008 and at $x/r_{LE} = -1$ for the NACA 0018. Different locations were used so that Amiet's prediction presented the best agreement with the numerical results for frequencies below 30 Hz. It is important to highlight that $\Lambda_{f,\infty} \gg r_{LE}$ for the NACA 0008 airfoil and $\Lambda_{f,\infty} \approx r_{LE}$ for the NACA 0018 airfoil, which might be the reason why different locations are needed to obtain more accurate WPF predictions since the ratio $\Lambda_{f,\infty}/r_{LE}$ dictates the mechanism responsible for the turbulence distortion.[20] The results are shown in Figs. 19 and 20 for the NACA 0008 and the NACA 0018, respectively. Figure 19 shows a better agreement of the Amiet(vK) prediction with the numerical and experimental spectra, mainly for frequencies below 30 Hz. For both airfoils, the difference between Amiet (vK)-Num. and numerical spectra was reduced from about 11 dB to less than 1 dB at 10 Hz when accounting for the turbulence distortion in the input parameters for the model. For Amiet(RDT)-Num., the differences were reduced from about 15 to 5 dB. For frequencies $f > 600$ Hz, a better agreement of the numerical spectra occurs with the Amiet(RDT)-Num. These results indicate that the disagreement of the Amiet prediction for positions close to the LE is most probably due to the turbulence distortion effects since the WPF is affected by this phenomenon. They also show that the turbulence parameters used as input to the model have to be representative of the turbulent flow in the region of interest. Thus, for a position close to the airfoil LE where the turbulence distortion is relevant, the distorted turbulence parameters near the position of interest should be used as input to the Amiet model for the WPF. However, the freestream turbulence parameters

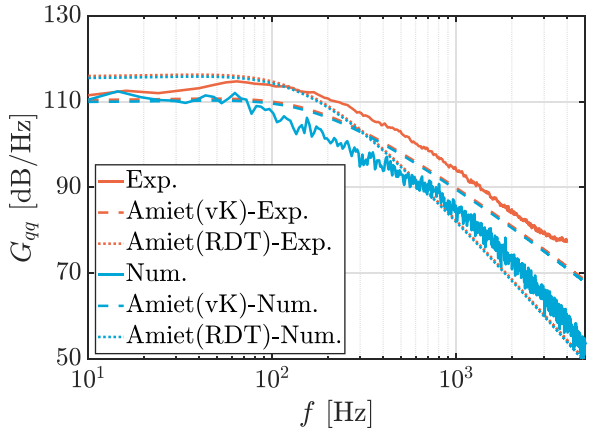

FIG. 19. PSD of the WPF on the NACA 0008 surface at $x/c = 0.0035$ and mid-span using as input to the prediction the turbulence parameters extracted at $x/r_{LE} = -2$. Num.—numerical results, Exp.—experimental results,[24] Amiet prediction—Eq. (2).

should be used as input for a position away from the LE where the turbulence distortion is negligible. Furthermore, the spectral level and main hump are sensitive to the turbulence input parameters, mainly the integral length scale. For example, the level difference in prediction of the Amiet(vK)-Num. for the cases where the inputs were the free-stream values and the distorted values is around 10 dB for $f = 30$ Hz.

E. Far-field noise

Figures 21 and 22 show the far-field noise from the simulations and predicted using the Amiet model for different directivity angles. The numerical far-field pressure fluctuations were calculated using the FW–H method, considering probes located at different angles in an arc with a radius of 1.5 m centered at the airfoil mid-chord and mid-span. An angle of 180° corresponds to an upstream position of the airfoil LE, and an angle of 0° corresponds to a downstream position of the airfoil trailing-edge. The Amiet model is calculated for two cases: (1) using the von Kármán turbulence spectrum with input Λ_f and u_{rms} extracted at $x/r_{LE} = 0$ without the airfoil, and (2) using the RDT-based turbulence spectrum with input Λ_f and u_{rms} extracted at $x/r_{LE} = -2$ with the airfoil. The position of $x/r_{LE} = -2$ is used because dos Santos *et al.*[24] showed that more accurate noise predictions are obtained when the turbulence input parameters are extracted at this position.

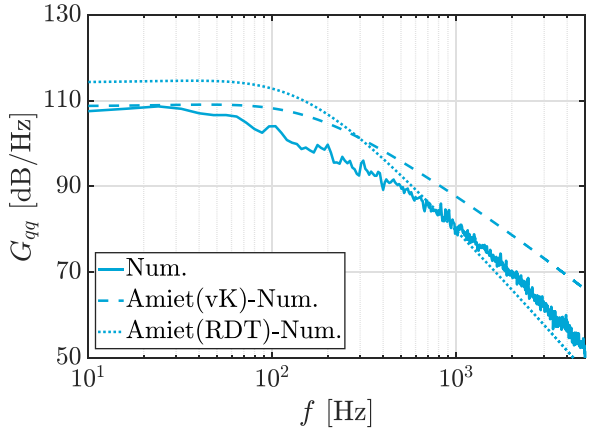

FIG. 20. PSD of the WPF on the NACA 0018 surface at $x/c = 0.0035$ and mid-span using as input to the prediction the turbulence parameters extracted at $x/r_{LE} = -1$. Num.—numerical results, Amiet prediction—Eq. (2).

We can observe in Fig. 21 humps that begin around $f \approx 1$ kHz. These are due to the interference between the noise emitted at the LE and the noise scattered over the trailing-edge. The CFD and von Kármán Amiet results are very similar in the frequencies and amplitudes of these humps, but some differences appear, as is evident at $\theta = 30°$. These differences are linked to the fact that Amiet theory assumes a flat plate. The results for the NACA 0018 airfoil are consistently further away from the Amiet results than the NACA 0008, which is compatible with the explanation of the differences coming mostly from the airfoil thickness. Analytical models tend to overpredict these humps, as the interference patterns occur without any dissipation or dispersion. Differences to Amiet results in the high-frequency humps have also been observed in experiments.[24]

For low frequencies ($f < 100$ Hz), the noise generated by both airfoils is similar. Figure 22 shows that the directivity at $f = 100$ Hz roughly resembles the directivity of a dipole because the airfoil is a compact noise source at this frequency, i.e., the acoustic wavelength is much larger than the airfoil chord. All analytical noise predictions (using Amiet's theory) overestimate the noise for frequencies around 100 Hz and underestimate the noise for lower frequencies ($f < 30$ Hz).

For frequencies between 100 Hz and around 1 kHz, the NACA 0018 radiates lower noise levels than the NACA 0008, as expected.[12,14,16] The directivity pattern for $f = 500$ Hz (see Fig. 22) shows that the NACA 0018 generates higher or at least comparable noise levels to the NACA 0008 for upstream positions, i.e., observer angles between 180° and 150°. However, as the observer angle decreases, the NACA 0018 generates lower noise levels than the NACA 0008, reaching a maximum difference of 10 dB at an angle of 30°. For this frequency ($f = 500$ Hz), the directivity pattern starts to deviate from a dipole because the airfoil is no longer a compact noise source. Regarding the noise prediction in the frequency range between 100 Hz and 1 kHz, it is clear that the prediction using the von Kármán model considerably overpredicts the noise, mainly for the thicker airfoil for observers localized at angles ranging from 30° to 120°; see Figs. 21 and 22. The noise prediction using the RDT-based spectrum also overpredicts the noise; however, it is closer to the numerical noise levels. Also, this noise prediction follows the trends of the numerical noise level; i.e., it predicts a lower noise level as the airfoil thickens. However, the RDT results do not predict the substantial change in the shape of the directivity pattern for $f = 500$ Hz for the NACA 0018 airfoil.

The noise radiated from both airfoils overlaps for higher frequencies ($f > 1$ kHz). However, the simulation results are questionable for $f > 2$ kHz. The directivity pattern at $f = 1$ kHz in Fig. 22 shows that the NACA 0018 noise level is higher than the NACA 0008 for upstream positions. However, this shifts for angles smaller than 150°, where the NACA 0018 produces lower noise levels. For angles smaller than 90°, the noise produced by both airfoils is comparable. Again, the Amiet prediction using the von Kármán model overpredicts the noise for all observer angles, whereas the prediction based on the RDT model approximates the airfoil noise better. Note that the RDT-based spectrum only changes the noise levels and does not affect the directivity

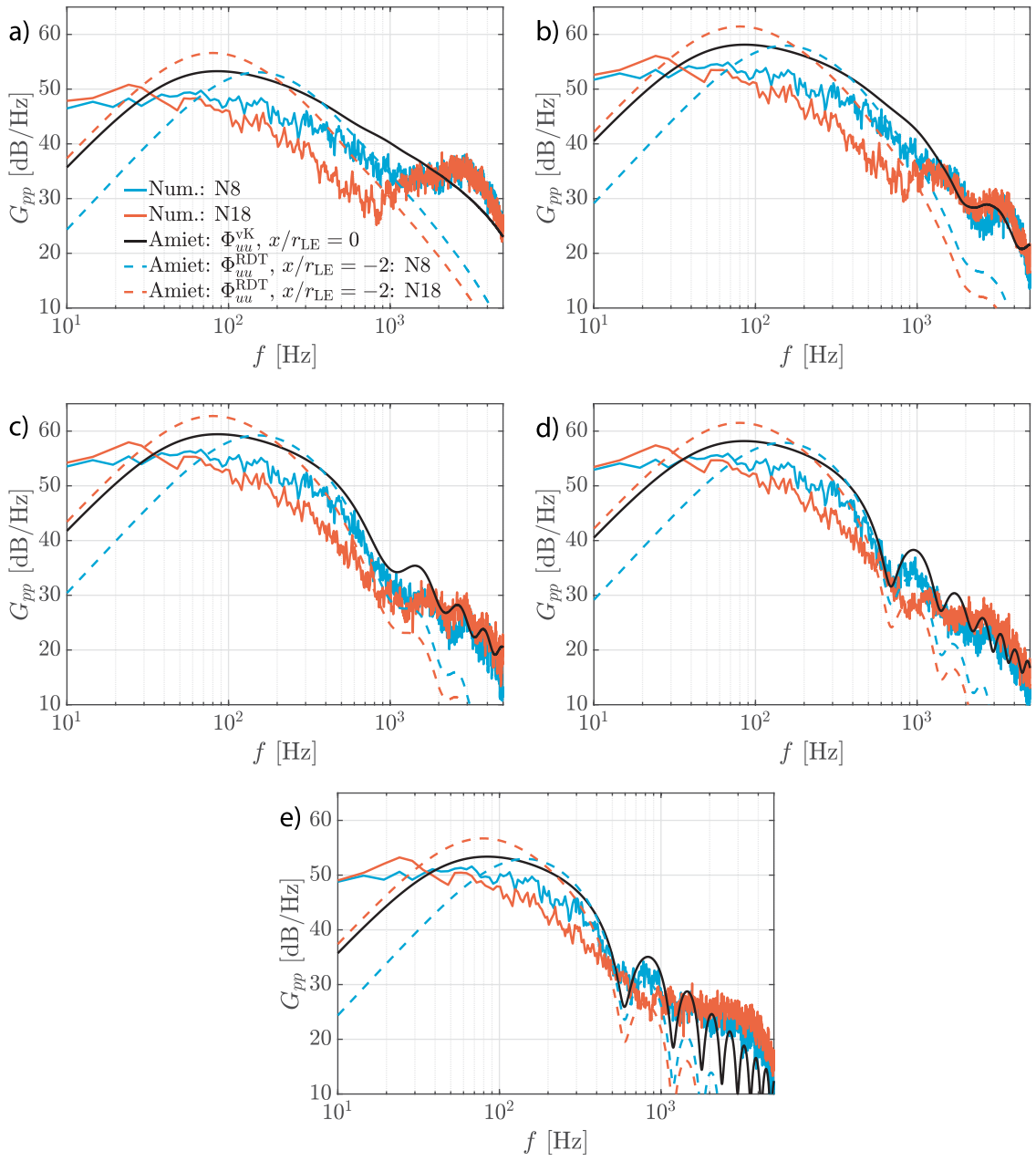

FIG. 21. PSD of the far-field noise for the NACA 0008 and NACA 0018 airfoils from the Amiet model and from the numerical results for directivity angles of 30° (a), 60° (b), 90° (c), 120° (d), and 150° (e).

pattern. Hence, modifying the turbulence spectrum is insufficient to account for the airfoil geometry effect on the directivity, requiring modifications to the airfoil response function. The directivity pattern for the thicker airfoil changes considerably compared with the prediction, whereas the pattern for the NACA 0008 roughly follows the prediction. Thus, the airfoil geometry in the LE region affects both the noise level and the directivity pattern.

To understand the change in the directivity due to the airfoil geometry, we now investigate the pressure fluctuations in the vicinity of the airfoil LE. The pressure coefficient $Cp = (p - p_\infty)/q_\infty$ was computed in the simulations, and its RMS Cp_{rms} is used as a way to compare the integral of the noise spectra for the two airfoils. Results are shown in Fig. 23, where we can observe that the pressure fluctuations start at the same level at $x/c = 0$ for both airfoils. However, the NACA 0008 shows a rise in Cp_{rms} soon after the LE, followed by a sharp decrease. In contrast, the NACA 0018 shows a decay in fluctuations immediately, though at a lower rate. The off-body pressure fluctuations can be seen in Fig. 24. The discontinuities observed in Cp_{rms}

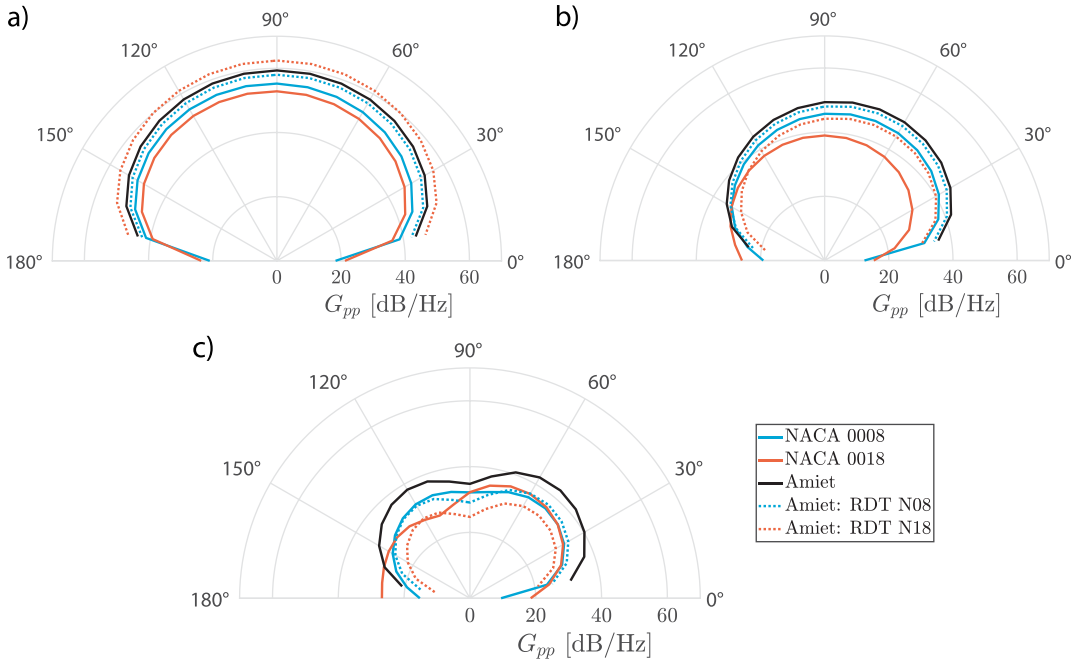

FIG. 22. Far-field noise directivity for the NACA 0008 and NACA 0018 airfoils from the Amiet model and from the numerical results for 100 Hz (a), 500 Hz (b), and 1000 Hz (c).

near the wall, mainly observed for the NACA 0018, are visualization artifacts and do not correspond to refinement interfaces. The NACA 0018 has pressure fluctuations mainly concentrated in front of its LE, while the pressure fluctuations near the NACA 0008 LE have a cardioid shape. This agrees with the far-field noise directivity patterns of the two airfoils: while the thinner airfoil shape agrees with the Amiet theory with noise levels at $\theta = 180°$ being very low, the thicker airfoil radiates noise upstream. The difference in the pressure fluctuations near the LE for these airfoils is likely associated with the higher concentration of transverse (z-direction) vortices that are observed just upstream of the NACA 0018 airfoil (Fig. 14), creating large spanwise velocity fluctuations.

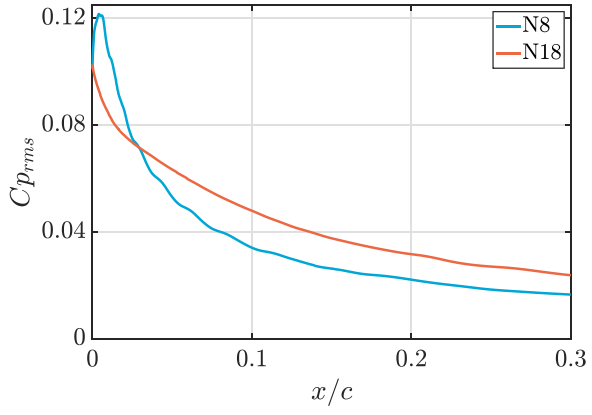

FIG. 23. RMS of the pressure coefficient at mid-span over the airfoil chord near the LE for the NACA 0008 and NACA 0018 airfoils.

F. Cutoff frequency discrepancies

The numerical mesh used in the freestream to resolve the incoming flow turbulence was shown to resolve fluctuations up to about 2 kHz (e.g., Figs. 6 and 8). Even for the case without any airfoil, the mesh is refined near the target airfoil LE position, but this was a small refinement region (Fig. 5), and the turbulence measured in that area had a similar cutoff as in the freestream (Fig. 8). Hence, at the LE location, there should be effectively no turbulence for $f > 2$ Hz.

Despite this, throughout this work, the WPF (Figs. 7 and 18) and far-field noise (Fig. 21) did not show a clear cutoff around 2 kHz. Instead, the spectra for these quantities showed slopes between 2 and 5 kHz that followed similar trends to experiments and analytical methods (again, see Figs. 18 and 21). This is evidence that the WPF and associated far-field noise above 2 kHz are not associated with the incoming freestream turbulence at the same frequencies. A clear example of this is comparing Figs. 6 and 7. At 5 kHz, the freestream turbulence is effectively zero, while the WPF at that frequency follows the expected slope.

A potential explanation for this is that the turbulence at $f < 2$ kHz creates smaller structures near the wall, hence far-field noise at $f = 5$ kHz. This goes against Amiet theory, where the noise is computed per frequency, meaning that far-field noise at 5 kHz only depends on the incoming turbulence spectrum at 5 kHz [see Eq. (1)]. This is surprising, and further research is needed to understand the reasons for this phenomenon.

VI. CONCLUSIONS AND OUTLOOK

In this work, we conducted LBM numerical simulations of grid-generated turbulence in a wind tunnel and analyzed the effect of two airfoils on the turbulent inflow and the LE noise generated.

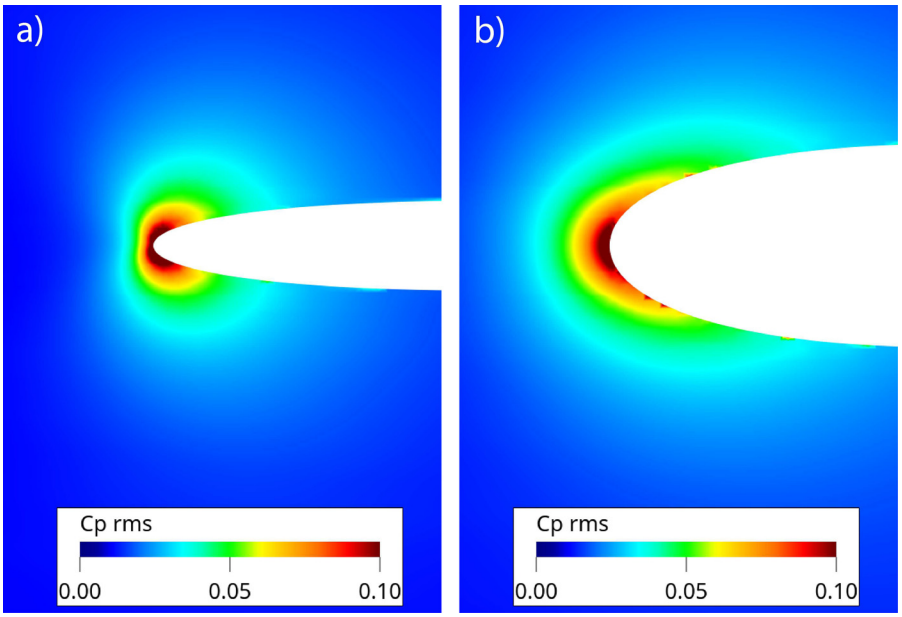

FIG. 24. Slice showing standard deviation pressure on the central plane for the NACA 0008 (a) and NACA 0018 (b) airfoils.

The simulations match the experimental data available in the literature and noise predictions based on the Amiet model reasonably well. The detailed flow data obtained with the simulations give valuable insight into the physics of LE noise generation for real airfoils.

The velocity fluctuations in the stagnation line of the thin airfoil ($\Lambda_f \gg r_{\mathrm{LE}}$) follow the RDT trends for cylinders. In this case, momentum is transferred from the streamwise velocity component to mainly the transverse component as the LE is approached, resulting in a decrease in the RMS of the streamwise velocity, an increase in the transverse component, and the spanwise component remains mostly constant. The momentum transfer between the streamwise and the transverse velocity results in the increase in energy for the large scales in the transverse direction. A different trend is observed when the turbulence length scale is slightly larger than the airfoil LE radius, i.e., $\Lambda_f > r_{\mathrm{LE}}$. For this case, the spanwise velocity fluctuations also increase as the LE is approached, whereas the transverse velocity fluctuations increase to a lesser extent. These results indicate that a different mechanism occurs when the turbulence length scale starts to be comparable to the airfoil LE radius. Furthermore, there are significant differences between the aerodynamics of thin and thick airfoils. The flow around the thick airfoil studied in this work has a concentration of vortices near the LE oriented in the transverse direction, creating high-velocity fluctuations in the spanwise direction. This phenomenon is not seen for the thin airfoil, where the transverse velocity fluctuations dominate near the LE. Regarding the scaling of the turbulence parameters at the stagnation line, the mean streamwise velocity scales with the streamwise position normalized by the airfoil thickness. Normalizing the streamwise position with the airfoil LE radius results in the scaling of the turbulence length scale for positions close to the airfoil LE ($x/r_{\mathrm{LE}} > -10$). However, the RMS streamwise velocity does not require normalizing the streamwise position, indicating that u_{rms} does not depend on the airfoil maximum thickness and LE radius. These results show that different flow quantities scale differently near the stagnation point.

The WPF close to the airfoil LE is mainly caused by the impingement of the turbulent inflow on the surface because the boundary layer is barely developed yet. However, at $x/c = 0.10$, the low-frequency spectral level is attributed to freestream turbulence, whereas the higher frequencies are attributed to the WPF induced by the boundary layer. The Amiet theory overpredicts the WPF spectra for chordwise positions close to the LE ($x/c = 0.0035$) because the turbulence is distorted for these positions, which is not considered in the model. By using the turbulence parameters near the LE as input to the model, a good agreement between the predicted WPF spectrum and the numerical spectrum is observed for low frequencies. For high frequencies, the numerical spectrum follows the decay predicted by the RDT for positions near the LE ($x/c = 0.0035$). At $x/c = 0.10$, the turbulence distortion does not affect the WPF spectrum significantly.

Regarding the far-field LE noise, the directivity pattern changes as the airfoil thickness increase, mainly for mid and high frequencies. Thicker airfoils radiate higher noise levels upstream of the LE than thin airfoils due to the drastic change in the WPF distribution near the LE. This considerable change is associated with the transverse (z-direction) vortices that are observed for thick airfoils, creating large spanwise velocity fluctuations. The difference between the numerical and the Amiet predicted directivity patterns grows with airfoil thickness and frequency. Moreover, using the RDT-based turbulence spectrum is expected to improve the Amiet prediction for far-field noise of airfoils. However, this was not observed here. The prediction using the RDT spectrum shows improved trends for the LE noise decreasing with the airfoil thickness compared to the von Kármán spectrum. However, using the RDT spectrum only scales the directivity noise levels, preserving the incorrect directivity patterns. Thus, the change in directivity patterns due to the airfoil thickness must be considered in the airfoil response function. Another potential limitation of Amiet models is that they assume noise at a certain frequency depends on the incoming turbulence at the same frequency only. In our results, we

observe WPF and far-field noise at expected levels for frequencies above what we resolve in the incoming turbulence. This should be a topic for further investigation.

As limitations in the Amiet models were shown for thick airfoils, numerical and experimental methods will continue to have value for applications including thick airfoils (such as those found in wind turbines) and less traditional applications, such as noise from complex LE shapes, which the current method is able to simulate.[77] This could be the case for highly eroded blades or to design airfoils with LE tubercles, which have been studied in various experiments due to their potential aerodynamic[78] and aeroacoustic[79,80] advantages over traditional shapes. In this work, we did not seek to isolate LE radius effects from airfoil thickness effects, as done by other authors.[12,14] Future studies could perform similar analyses as we conducted here while separating the effects of LE radius and airfoil thickness.

ACKNOWLEDGMENTS

The authors would like to thank the members of the PANPA project, which is in collaboration with TNO and the Maritime Research Institute Netherlands (MARIN), for the feedback on this research.

AUTHOR DECLARATIONS

Conflict of Interest

The authors have no conflicts to disclose.

Author Contributions

André F. P. Ribeiro: Conceptualization (equal); Data curation (equal); Formal analysis (equal); Investigation (lead); Methodology (equal); Resources (lead); Software (equal); Validation (supporting); Visualization (equal); Writing – original draft (equal). **Fernanda Leticia dos Santos:** Conceptualization (equal); Data curation (equal); Formal analysis (equal); Investigation (supporting); Methodology (equal); Software (equal); Validation (lead); Visualization (equal); Writing – original draft (equal). **Kees Venner:** Funding acquisition (equal); Project administration (lead); Resources (supporting); Supervision (equal); Writing – review & editing (equal). **Leandro Dantas de Santana:** Funding acquisition (equal); Supervision (equal); Writing – review & editing (equal).

DATA AVAILABILITY

The data that support the findings of this study are available from the corresponding author upon reasonable request.

REFERENCES

[1]K. Abrahamsen, "The ship as an underwater noise source," Proc. Meet. Acoust. **17**, 070058 (2012).
[2]R. E. Kurt, H. Khalid, O. Turan, M. Houben, J. Bos, and I. H. Helvacioglu, "Towards human-oriented norms: Considering the effects of noise exposure on board ships," Ocean Eng. **120**, 101–107 (2016).
[3]T. Götz, G. Hastie, L. Hatch, O. Raustein, B. Southall, M. Tasker, F. Thomsen, J. Campbell, and B. Fredheim, "Overview of the impacts of anthropogenic underwater sound in the marine environment," Technical Report No. 441/2009, OSPAR Convention, Convention for the Protection of the Marine Environment of the North-East Atlantic, 2009.
[4]M. C. Zwart, J. C. Dunn, P. J. K. McGowan, and M. J. Whittingham, "Wind farm noise suppresses territorial defense behavior in a songbird," Behav. Ecol. **27**, 101–108 (2016).
[5]R. K. Amiet, "Noise due to turbulent flow past a trailing edge," J. Sound Vib. **47**, 387–393 (1976).
[6]J. S. Carlton, *Marine Propellers and Propulsion* (Butterworth-Heinemann, 2018).
[7]S. Merz, R. Kinns, and N. Kessissoglou, "Structural and acoustic responses of a submarine hull due to propeller forces," J. Sound Vib. **325**, 266–286 (2009).
[8]W. J. Devenport, J. K. Staubs, and S. A. L. Glegg, "Sound radiation from real airfoils in turbulence," J. Sound Vib. **329**, 3470–3483 (2010).
[9]S. Moreau, M. Roger, and V. Jurdic, "Effect of angle of attack and airfoil shape on turbulence-interaction noise," AIAA Paper No. 2005-2973, 2005.
[10]J. Gershfeld, "Leading edge noise from thick foils in turbulent flows," J. Acoust. Soc. Am. **116**, 1416–1426 (2004).
[11]S. Oerlemans and P. Migliore, "Aeroacoustic wind tunnel tests of wind turbine airfoils," AIAA Paper No. 2004-3042, 2004.
[12]J. Gill, X. Zhang, and P. Joseph, "Symmetric airfoil geometry effects on leading edge noise," J. Acoust. Soc. Am. **134**, 2669–2680 (2013).
[13]J. Han, Y. Zhang, S. Li, W. Hong, and D. Wu, "On the reduction of the noise in a low-pressure turbine cascade associated with the wavy leading edge," Phys. Fluids **35**, 095103 (2023).
[14]T. Hainaut, G. Gabard, and V. Clair, "A CAA study of turbulence distortion in broadband fan interaction noise," AIAA Paper No. 2016-2839, 2016.
[15]L. J. Ayton and P. Chaitanya, "Analytical and experimental investigation into the effects of leading-edge radius on gust–aerofoil interaction noise," J. Fluid Mech. **829**, 780–808 (2017).
[16]C. Paruchuri, "Aerofoil geometry effects on turbulence interaction noise," Ph.D. thesis (University of Southampton, 2017).
[17]R. W. Paterson and R. K. Amiet, "Acoustic radiation and surface pressure characteristics of an airfoil due to incident turbulence," Contractor Report No. CR-2733, NASA, 1976.
[18]A. Piccolo, R. Zamponi, F. Avallone, and D. Ragni, "Turbulence-distortion analysis for leading-edge noise-prediction enhancement," AIAA Paper No. 2023-3628, 2023.
[19]R. Zamponi, S. Satcunanathan, S. Moreau, D. Ragni, M. Meinke, W. Schröder, and C. Schram, "On the role of turbulence distortion on leading-edge noise reduction by means of porosity," J. Sound Vib. **485**, 115561 (2020).
[20]J. C. R. Hunt, "A theory of turbulent flow round two-dimensional bluff bodies," J. Fluid Mech. **61**, 625–706 (1973).
[21]R. E. Britter, J. C. R. Hunt, and J. C. Mumford, "The distortion of turbulence by a circular cylinder," J. Fluid Mech. **92**, 269–301 (1979).
[22]P. F. Mish and W. J. Devenport, "An experimental investigation of unsteady surface pressure on an airfoil in turbulence–Part 2: Sources and prediction of mean loading effects," J. Sound Vib. **296**, 447–460 (2006).
[23]F. L. dos Santos, L. Botero-Bolivar, C. H. Venner, and L. D. de Santana, "Modeling the turbulence spectrum dissipation range for leading-edge noise prediction," AIAA J. **60**, 3581–3592 (2022).
[24]F. L. dos Santos, L. Botero-Bolívar, C. H. Venner, and L. D. de Santana, "Inflow turbulence distortion for airfoil leading-edge noise prediction for large turbulence length scales for zero-mean loading," J. Acoust. Soc. Am. **153**, 1811–1822 (2023).
[25]L. D. de Santana, J. Christophe, C. Schram, and W. Desmet, "A rapid distortion theory modified turbulence spectra for semi-analytical airfoil noise prediction," J. Sound Vib. **383**, 349–363 (2016).
[26]L. Bowen, A. Celik, and M. Azarpeyvand, "A thorough experimental investigation on airfoil turbulence interaction noise," Phys. Fluids **35**, 035123 (2023).
[27]S. A. L. Glegg and W. J. Devenport, "Panel methods for airfoils in turbulent flow," J. Sound Vib. **329**, 3709–3720 (2010).
[28]M. J. Groom, B. Y. Zhou, and Q. Wang, "Efficient prediction of leading edge noise with a synthetic turbulence approach," AIAA Paper No. 2022-2819, 2022.
[29]J. Delfs, J. Yin, and X. Li, "Leading edge noise studies using CAA," AIAA Paper No. 1999-1897, 1999.
[30]C. Paruchuri, N. Subramanian, P. Joseph, C. Vanderwel, J. Turner, J. W. Kim, and B. Ganapathisubramani, "Broadband noise reduction through leading edge serrations on realistic aerofoils," AIAA Paper No. 2015-2202, 2015.

[31]M. Buszyk, C. Polacsek, R. Barrier, T. L. Garrec, and C. Bailly, "3D CAA methodology using synthetic turbulence to assess turbulence-cascade interaction noise emission and reduction from serrated airfoils," AIAA Paper No. 2021-2257, 2021.
[32]D. Casalino, A. Hazir, and A. Mann, "Turbofan broadband noise prediction using the lattice Boltzmann method," AIAA J. **56**, 609–628 (2018).
[33]S. A. Petrikat, R. Karve, and D. Angland, "Broadband leading edge interaction noise prediction using simulated grid turbulence," AIAA Paper No. 2018-3286, 2018.
[34]L. Trascinelli, L. Bowen, A. Piccolo, F. Avallone, R. Zamponi, D. Ragni, B. Zang, and B. Y. Zhou, "Numerical simulation of grid-generated turbulence interaction with a NACA0012 airfoil," AIAA Paper No. 2023-3633, 2023.
[35]S. Succi, *The Lattice Boltzmann Equation: For Fluid Dynamics and Beyond* (Clarendon Press, 2001).
[36]L. Mieussens, "A survey of deterministic solvers for rarefied flows (Invited)," AIP Conf. Proc. **1628**, 943–951 (2014).
[37]P. J. Dellar, "An interpretation and derivation of the lattice Boltzmann method using strang splitting," Comput. Math. Appl. **65**, 129–141 (2013).
[38]P. L. Bhatnagar, E. P. Gross, and M. Krook, "A model for collision processes in gases. I. Small amplitude processes in charged and neutral one-component systems," Phys. Rev. **94**, 511–525 (1954).
[39]M. R. Khorrami, B. Konig, E. Fares, A. Ribeiro, M. Czech, and P. A. Ravetta, "Airframe noise simulations of a full-scale large civil transport in landing configuration," AIAA Paper No. 2021-2161, 2021.
[40]H. Chen, C. Teixeira, and K. Molvig, "Realization of fluid boundary conditions via discrete Boltzmann dynamics," Int. J. Mod. Phys. C **09**, 1281–1292 (1998).
[41]A. Anagnost, A. Alajbegovic, H. Chen, D. Hill, C. Teixeira, and K. Molvig, "Digital physics^{TM} analysis of the morel body in ground proximity," SAE Trans. **106**, 306–312 (1997).
[42]E. Fares, B. Duda, A. F. P. Ribeiro, and B. König, "Scale-resolving simulations using a lattice Boltzmann-based approach," CEAS Aeronaut. J. **9**, 721 (2018).
[43]J. P. Boris, F. F. Grinstein, E. S. Oran, and R. L. Kolbe, "New insights into large eddy simulation," Fluid Dyn. Res. **10**, 199–228 (1992).
[44]H. Chen, S. Chen, and W. H. Matthaeus, "Recovery of the Navier–Stokes equations using a lattice-gas Boltzmann method," Phys. Rev. A **45**, R5339–R5342 (1992).
[45]P. J. Dellar, "Lattice Boltzmann algorithms without cubic defects in galilean invariance on standard lattices," J. Comput. Phys. **259**, 270–283 (2014).
[46]G. Zhao-Li, Z. Chu-Guang, and S. Bao-Chang, "Non-equilibrium extrapolation method for velocity and pressure boundary conditions in the lattice Boltzmann method," Chin. Phys. **11**, 366 (2002).
[47]G. Brès, F. Pérot, and D. Freed, "Properties of the lattice Boltzmann method for acoustics," AIAA Paper No. 2009-3395, 2009.
[48]E. Manoha and B. Caruelle, "Summary of the LAGOON solutions from the benchmark problems for airframe noise computations-III workshop," AIAA Paper No. 2015-2846, 2015.
[49]A. Aniello, D. Schuster, P. Werner, J. Boussuge, M. Gatti, C. Mirat, L. Selle, T. Schuller, T. Poinsot, and U. Rüde, "Comparison of a finite volume and two lattice Boltzmann solvers for swirled confined flows," Comput. Fluids **241**, 105463 (2022).
[50]A. F. P. Ribeiro and C. Muscari, "Sliding mesh simulations of a wind turbine rotor with actuator line lattice-Boltzmann method," Wind Energy (published online, 2023).
[51]G. A. Brès, D. Freed, M. Wessels, S. Noelting, and F. Pérot, "Flow and noise predictions for the tandem cylinder aeroacoustic benchmark," Phys. Fluids **24**, 036101 (2012).
[52]A. F. P. Ribeiro, D. Casalino, and E. Fares, "Lattice-Boltzmann simulations of an oscillating NACA0012 airfoil in dynamic stall," in *Advances in Fluid-Structure Interaction*, edited by M. Braza, A. Bottaro, and M. Thompson (Springer International Publishing, 2016), pp. 179–192.
[53]A. F. P. Ribeiro, D. Casalino, E. Fares, and M. Choudhari, "Direct numerical simulation of an airfoil with sand grain roughness on the leading edge," Technical Memorandum No. NASA/TM-2016-219363, NASA, 2016.
[54]G. Romani, D. Casalino, and W. van der Velden, "Numerical analysis of airfoil trailing-edge noise for straight and serrated edges at incidence," AIAA J. **59**, 2558–2577 (2021).
[55]F. Avallone, W. C. P. van der Velden, D. Ragni, and D. Casalino, "Noise reduction mechanisms of sawtooth and combed-sawtooth trailing-edge serrations," J. Fluid Mech. **848**, 560–591 (2018).
[56]G. Brès, F. Pérot, and D. Freed, "A Ffowcs Williams–Hawkings solver for lattice-Boltzmann based computational aeroacoustics," AIAA Paper No. 2010-3711, 2010.
[57]J. E. Ffowcs Williams and D. L. Hawkings, "Sound generation by turbulence and surfaces in arbitrary motion," Philos. Trans. R. Soc., A **264**, 321–342 (1969).
[58]F. Farassat and G. P. Succi, "A review of propeller discrete frequency noise prediction technology with emphasis on two current methods for time domain calculations," J. Sound Vib. **71**, 399–419 (1980).
[59]K. S. Brentner, "Prediction of helicopter rotor discrete frequency noise: A computer program incorporating realistic blade motions and advanced acoustic formulation," Technical Memorandum No. 87721, National Aeronautics and Space Administration, 1986.
[60]D. Casalino, "An advanced time approach for acoustic analogy predictions," J. Sound Vib. **261**, 583–612 (2003).
[61]F. Farassat, "Derivation of formulations 1 and 1a of Farassat," Technical Memorandum No. 214853, National Aeronautics and Space Administration, 2007.
[62]A. F. P. Ribeiro, M. R. Khorrami, R. Ferris, B. König, and P. A. Ravetta, "Lessons learned on the use of data surfaces for Ffowcs Williams–Hawkings calculations: Airframe noise applications," Aerosp. Sci. Technol. **135**, 108202 (2023).
[63]R. K. Amiet, "Acoustic radiation from an airfoil in a turbulent stream," J. Sound Vib. **41**, 407–420 (1975).
[64]L. D. de Santana, "Semi-analytical methodologies for airfoil noise prediction," Ph.D. thesis (KU Leuven, 2015).
[65]P. F. Mish and W. J. Devenport, "An experimental investigation of unsteady surface pressure on an airfoil in turbulence–Part 1: Effects of mean loading," J. Sound Vib. **296**, 417–446 (2006).
[66]S. Glegg and W. Devenport, *Aeroacoustics of Low Mach Number Flows* (Academic Press, London, UK, 2017).
[67]L. de Santana, M. P. J. Sanders, and C. H. Venner, "The UTwente aeroacoustic wind tunnel upgrade," AIAA Paper No. 2018-3136, 2018.
[68]P. Welch, "The use of fast Fourier transform for the estimation of power spectra: A method based on time averaging over short, modified periodograms," IEEE Trans. Audio Electroacoust. **15**, 70–73 (1967).
[69]J. O. Hinze, *Turbulence* (McGraw–Hill, New York, USA, 1975).
[70]G. I. Taylor, "The spectrum of turbulence," Proc. R. Soc. London, Ser. A **164**, 476–490 (1938).
[71]S. B. Pope, *Turbulent Flows* (Cambridge University Press, Cambridge, United Kingdom, 2000) pp. 182–263.
[72]C. C. Lin, "On Taylor's hypothesis and the acceleration terms in the Navier–Stokes equations," Q. Appl. Math. **10**, 295–306 (1953).
[73]A. Trush, S. Pospisil, and H. Kozmar, "Comparison of turbulence integral length scale determination methods," WIT Trans. Eng. Sci. **128**, 113–123 (2020).
[74]A. F. P. Ribeiro, "Unsteady analysis of ground vortex ingestion with LBM-VLES," AIAA Paper No. 2022-0244, 2022.
[75]E. Dogan, R. E. Hanson, and B. Ganapathisubramani, "Interactions of large-scale free-stream turbulence with turbulent boundary layers," J. Fluid Mech. **802**, 79–107 (2016).
[76]L. Botero-Bolívar, F. L. dos Santos, C. H. Venner, and L. de Santana, "Increase of unsteady pressure at a trailing edge due to inflow turbulence," AIAA J. **60**, 6798–6813 (2022).
[77]A. F. P. Ribeiro, D. Singh, B. Konig, and E. Fares, "On the stall characteristics of iced wings," AIAA Paper No. 2017-1426, 2017.
[78]V. Demirci, M. Seyhan, and M. Sarioglu, "Investigation of aerodynamic performance of Clark-Y airfoil with more realistic tubercle model and internal slots," Phys. Fluids **35**, 087109 (2023).
[79]R. I. A. Simanto, J.-W. Hong, K.-S. Kim, B.-K. Ahn, and S. Shin, "Experimental investigation on cavitation and induced noise of two-dimensional hydrofoils with leading-edge protuberances," Phys. Fluids **34**, 124115 (2022).
[80]S. K. Singh and S. Narayanan, "On the reductions of airfoil–turbulence noise by curved wavy serrations," Phys. Fluids **35**, 075140 (2023).